J. Fluid Mech. (2011), *vol.* 675, *pp.* 168–198.
doi:10.1017/S0022112011000127

Lagrangian mixing in straight compound channels

ALESSANDRO STOCCHINO[1]†, GIOVANNI BESIO[1], SONIA ANGIOLANI[1] AND MAURIZIO BROCCHINI[2]

[1]Dipartimento di Ingegneria delle Costruzioni, dell'Ambiente e del Territorio, University of Genova, Genova 16145, Italy

[2]Department ISAC, Polytechnic University of Marche, Via Brecce Bianche, 12, 60131 Ancona, Italy

(Received 9 July 2010; revised 22 October 2010; accepted 26 December 2010; first published online 29 March 2011)

Recently Stocchino & Brocchini (*J. Fluid Mech.*, vol. 643, 2010, p. 425 have studied the dynamics of two-dimensional (2D) large-scale vortices with vertical axis evolving in a straight compound channel under quasi-uniform flow conditions. The mixing processes associated with such vortical structures are here analysed through the results of a dedicated experimental campaign. Time-resolved Eulerian surface velocity fields, measured using a 2D particle-image velocimetry system, form the basis for a Lagrangian analysis of the dispersive processes that occur in compound channels when the controlling physical parameters, i.e. the flow depth ratio (r_h) and the Froude number (Fr) are changed. Lagrangian mixing is studied by means of various approaches based either on single-particle or multiple-particle statistics (relative and absolute statistics, probability density functions (p.d.f.s) of relative displacements and finite-scale Lyapunov exponents). Absolute statistics reveal that transitional macrovortices, typical of shallow flow conditions, strongly influence the growth in time of the total absolute dispersion, after the initial ballistic regime, leading to a non-monotonic behaviour. In deep flow conditions, on the contrary, the absolute dispersion displays a monotonic growth because the generation of transitional macrovortices does not take place. In all cases an asymptotic diffusive regime is reached.

Multiple-particle dynamics is controlled by r_h and Fr. Different growth regimes of the relative diffusivity have been found depending on the flow conditions. This behaviour can be associated with different energy transfer processes and it is further confirmed by the p.d.f.s of relative displacements, which show a different asymptotical shape depending on the separation scales and the Froude number. Finally, an equilibrium regime is observed for all the experiments by analysing the decay of the finite-scale Lyapunov exponents with the particle separations.

Key words: mixing and dispersion, river dynamics, shallow water flows

1. Introduction

Natural rivers commonly exhibit cross-stream sections composed of a deep main channel and shallow floodplains; hence, they are called 'compound channels'. The compound channel geometry is often artificially created in many applications of

† Email address for correspondence: jorma@dicat.unige.it

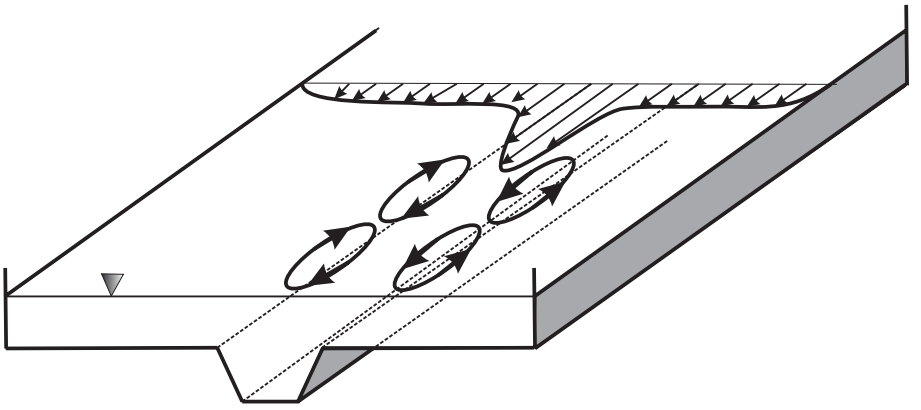

FIGURE 1. Graphical illustration of the compound channel flow showing macrovortices in the transition regions and mean flow velocity distribution along the transversal coordinate.

river engineering (Shiono & Knight 1991; van Prooijen, Battjes & Uijttewaal 2005), trying to restore a natural shape. In the last two decades, a major effort has been dedicated to understand the dynamics of uniform and non-uniform flows evolving in compound channels with the aim to better model the fundamental processes. Uniform compound channel flows are often studied using the conceptual scheme of Shiono & Knight (1991); see figure 1 for a graphical illustration of the flow. The overall flow is, in general, a complicated three-dimensional (3D) turbulent flow. However, the main agents of transport of momentum and mass between the main channel and the floodplains are found to be the quasi-two-dimensional (2D) macrovortices (with vertical axes) generated at the transition region, where there is an intense generation of vorticity owing to the flow depth jump (Soldini *et al.* 2004). Secondary flows are, usually, disregarded since they have a major effect in a confined region, close to the bottom, of the main channel. For this reason, many authors have chosen to apply a 2D analysis based on the shallow-water approximation (Sellin 1964; Shiono & Knight 1991; Nezu, Onitsuka & Iketani 1999; van Prooijen & Uijttewaal 2002, among others). The 'shallow flow' assumption is applied not only to compound channel flows but also to a variety of other flows which are globally shallow (e.g. jet and wakes) but still retain local vertical gradients (e.g. flows around groin fields), as described in Jirka (2001); Socolofksy & Jirka (2004) and Nikora *et al.* (2007).

Recently, Stocchino & Brocchini (2010) have presented a statistical analysis of the properties of quasi-2D macrovortices that are formed at the transition region of a compound channel, showing that the typical size of these structures, after their initial growth, remains constant in the streamwise direction. This was related to the fact that the topographic forcing, i.e. the depth jump between the main channel and the floodplains, being the main production mechanism of large-scale vorticity, was constant in the same direction. The possible consequences on mass transport processes were only outlined. However, the understanding of the role of coherent vortices on mass transport is of particular interest: floodplains of natural rivers are often wetlands with abundant wild life and the knowledge of the mass transport processes is vital to preserve the environmental conditions. In this respect, the above-mentioned macrovortices play a fundamental role in the transverse exchange of mass (e.g. pollutants and nutrients) between the main channel and the floodplains

(van Prooijen & Uijttewaal 2002). In general, coherent structures are commonly recognized as major agents of mass transport, also owing to their ability to trap mass and to inhibit exchanges among different flow regions. Interesting reviews on this subject are those of Provenzale (1999), Boffetta *et al.* (2001) and LaCasce (2008).

The present contribution focuses on the mixing processes that occur in a uniform compound channel, assuming a shallow-water conceptual model. In this sense, the following Lagrangian analysis can be regarded as a natural extension of the study by Stocchino & Brocchini (2010), who restricted their attention only to the Eulerian characteristics of the flow. As in many other applications concerned with geophysical flows (Morel & Bandeen 1973; Er-El & Peskin 1981; Orre, Gjevik & LaCasce 2006; Garcia-Olivares, Isern-Fontanet & Garcia-Ladona 2007; LaCasce 2008), the turbulent flows of interest can be regarded as quasi-2D, considering secondary flows in the cross-sections of minor importance. Hence, we interpret the experimental measurements relying on results valid for pure 2D turbulence, making, whenever possible, a close analogy with such results.

From the measurements of time-dependent, two-dimensional surface Eulerian velocity fields, we first analyse the flow by means of a dynamical partitioning based on the Hua & Kline (1998) criterion, which defines flow regions with different mixing properties. We then perform a numerical integration of sets of particle trajectories starting from the Eulerian velocity fields obtained from the particle-image velocimetry (PIV) technique, for each experiment. The particle trajectories form the basis for the Lagrangian analysis of the mixing processes described in § 4. The resulting absolute and relative dispersion and diffusivity are discussed in detail to describe the mixing processes and the analysis is classified by means of finite-scale Lyapunov exponents (FSLEs). Section 5 closes the paper.

2. The experiments

The present experiments have been carried out using the same apparatus as described in Stocchino & Brocchini (2010), suitably modified to enable changes in the bed longitudinal slope (S).

Here, we briefly recall the main characteristics of the apparatus and the measuring system. The flume is 20 m long, 56 cm wide with a trapezoidal cross-section composed of a central main channel ($W^*_{mc} = 20$ cm), two lateral flat floodplains ($W^*_{fp} = 18$ cm) and a transition region ($W^*_{tr} = 2.5$ cm). A sketch of the cross-section of the experimental flume is shown in figure 2. Asterisks identify dimensional quantities. A Cartesian coordinate system is used in which the x^*- and y^*-axes are aligned with the streamwise and spanwise directions of the flow, respectively. In the following, horizontal distances are normalized by the main channel half-width ($W^*_{mc}/2 = 10$ cm). More appropriate scales are used to make dimensionless the results of the mixing analysis. This is further detailed in § 4.2. As discussed in Stocchino & Brocchini (2010), the turbulent flow is completely developed after a distance downstream of the inlet of about 6.5 m. In the present study, we have focussed our attention only on fully developed turbulent conditions, choosing the measuring area at a distance of 10 m downstream of the flume inlet.

In table 1, we summarize the main experimental parameters, providing the values of the ratio between the main channel water depth and that of the floodplains, $r_h = h^*_{mc}/h^*_{fp}$, the Froude number, $Fr = U^*_m/\sqrt{gR^*}$, where R^* is the hydraulic radius, g is gravity and U^*_m is the peak velocity in the main channel, the liquid discharge (Q^*)

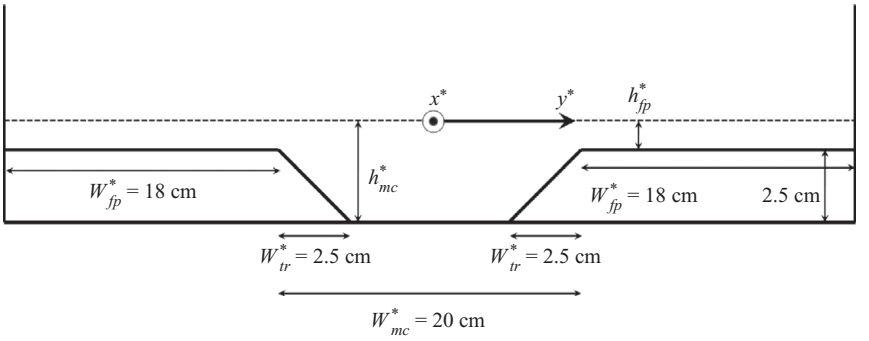

FIGURE 2. Sketch of the cross-section of the flume.

and the Reynolds number $Re = 4U^*_m R^*/\nu$, where ν is the kinematic viscosity. About 50 experiments have been performed changing the main parameters (Fr and r_h) that are grouped in table 1 depending on the flow regimes as suggested by Nezu *et al.* (1999). Moreover, the experiments belonging to each class are listed according to the decreasing value of the longitudinal bed slope (S).

Two-dimensional surface velocity measurements have been obtained using the same PIV system as that of Stocchino & Brocchini (2010), which consists of a high-speed digital camera (IDT model Xs3) and an illumination system composed of three white light incandescent lamps of 1000 W. The seeding tracers were white plastic particles with a mean diameter of 150 μm and a specific gravity of about 1.05. Anti-clustering treatments have been preventatively applied to the particles. The approximate area density of the particle tracers was estimated at 10 particles cm^{-2}. For the present purposes, the area of interest of the velocity measurements has been increased with respect to the experimental results already presented by the authors. In fact, as described below, the Eulerian velocity fields are used as the basis for the computation of trajectories and, for this task, a longer domain is needed to ensure an acceptable accuracy of the Lagrangian statistics. Therefore, the area of interest was a rectangle with dimensions up to $(1.2 \times 0.6)\,m^2$. The image-repetition rate was chosen between 100 and 250 Hz, depending on the flow velocity and a single acquisition was made of a number of frames between 2000 and 4000, resulting in different temporal intervals from 10 to 45 s. To test the repeatability of the measurements, we have performed several acquisitions for a fixed set of experimental parameters (r_h, Fr). Finally, probability density functions (p.d.f.s) of the measured displacements have been calculated to test whether the PIV set-up in use was adequate to avoid peak-locking effects, which may deteriorate the quality of the measurements. The resulting p.d.f.s, not being multimodal, suggest that the measured velocity is not affected by such a systematic error.

The present experimental approach, based on the free-surface velocity measurement, is often used in many experimental works with primary focus on quasi-2D vortical structures (see Jirka 2001; Socolofksy & Jirka 2004; Nikora *et al.* 2007, among others). This approach is valid as long as secondary flows, which develop over vertical cross-sections of the flow, can be considered negligible in the formation of the quasi-2D macrovortices at hand.

In the following, results are analysed with reference to the classification introduced by Nezu *et al.* (1999). 'Shallow flows' ($r_h > 3$) are characterized by monotonic velocity

Experiment	r_h (−)	Fr (−)	S (−)	Q^* (l s^{-1})	U_m^* (m s^{-1})	$Re \times 10^4$ (−)
			Shallow flows			
EXP101	3.70	0.88	0.0064	4.88	0.34	28.2
EXP102	3.23	0.91	0.0064	5.79	0.35	32.5
EXP04	3.69	0.87	0.0064	4.88	0.34	28.2
EXP06.1	3.10	0.92	0.0064	6.14	0.36	33.8
EXP010	4.42	0.73	0.0048	3.55	0.18	12.8
EXP011	3.50	0.77	0.0048	4.62	0.20	17.3
EXP012	3.40	0.80	0.0048	5.25	0.22	19.5
EXP201	4.16	0.60	0.0032	2.99	0.27	20.1
EXP202	3.60	0.62	0.0032	3.55	0.29	24.5
EXP203	3.36	0.64	0.0032	3.9	0.31	27.8
EXP204	3.08	0.65	0.0032	4.37	0.32	30.6
EXP001	3.69	0.44	0.0016	2.39	0.17	13.7
EXP002	3.43	0.46	0.0016	3.03	0.19	16.3
EXP003	3.05	0.47	0.0016	3.49	0.20	19.8
			Intermediate flows			
EXP103	2.62	0.97	0.0064	8.01	0.42	48.5
EXP104	2.29	1.03	0.0064	10.35	0.51	69.6
EXP105	2.15	1.05	0.0064	11.85	0.56	84.9
EXP106	2.07	1.07	0.0064	12.81	0.58	93.1
EXP107	2.03	1.07	0.0064	13.84	0.60	99.8
EXP06.6	2.92	0.94	0.0064	6.68	0.36	36.9
EXP07	2.71	0.96	0.0064	7.56	0.37	41.1
EXP10	2.32	1.02	0.0064	10.01	0.49	66.2
EXP12	2.11	1.06	0.0064	12.36	0.53	82.9
EXP13	2.02	1.07	0.0064	13.54	0.57	95.2
EXP013	2.36	0.84	0.0048	6.54	0.25	33.1
EXP014	2.30	0.87	0.0048	8.09	0.26	35.6
EXP015	2.10	0.92	0.0048	10.75	0.38	59.7
EXP205	2.57	0.69	0.0032	5.85	0.35	41.4
EXP206	2.40	0.71	0.0032	6.68	0.36	46.6
EXP207	2.26	0.73	0.0032	7.47	0.37	51.8
EXP208	2.16	0.74	0.0032	8.26	0.38	57.2
EXP209	2.04	0.76	0.0032	9.44	0.42	69.4
EXP004	2.61	0.50	0.0016	4.32	0.21	23.8
EXP005	2.40	0.51	0.0016	5.01	0.23	29.8
EXP006	2.20	0.53	0.0016	5.89	0.27	39.6
			Deep flows			
EXP108	1.95	1.09	0.0064	14.76	0.64	11.4
EXP109	1.86	1.11	0.0064	16.82	0.69	13.5
EXP110	1.82	1.12	0.0064	17.82	0.70	14.3
EXP112	1.28	0.14	0.0064	7.28	0.20	14.2
EXP14	1.96	1.09	0.0064	14.67	0.59	104.2
EXP16	1.85	1.12	0.0064	16.99	0.63	124.1
EXP17	1.82	1.13	0.0064	17.94	0.64	131.3
EXP017	1.85	0.96	0.0048	14.29	0.44	86.9
EXP018	1.82	0.99	0.0048	16.66	0.49	99.8
EXP210	1.90	0.78	0.0032	11.31	0.45	85.0
EXP211	1.82	0.79	0.0032	12.48	0.48	97.6
EXP212	1.73	0.81	0.0032	14.53	0.51	116.1
EXP213	1.68	0.82	0.0032	16.07	0.53	130.1
EXP007	1.97	0.55	0.0016	7.74	0.28	48.2
EXP008	1.83	0.56	0.0016	8.99	0.30	60.0
EXP009	1.77	0.57	0.0016	9.87	0.24	52.1

TABLE 1. Main experimental parameters.

profiles and strong velocity gradients at the transition between the main channel and the floodplains, leading to a strong shearing in the transition, associated with intense macrovortices. At the wall boundary layers, only a weak shear occurs and almost no macrovortices are generated. 'Intermediate flows' ($2 < r_h < 3$) are characterized by non-monotonic velocity profiles with a dip over the transition. According to Nezu *et al.* (1999), such an effect is the signature of counter-rotating macrovortices at the transition. The depth increase leads to a growth of the wall boundary-layer thickness, and macrovortices are also generated, by wall-adherence-induced shearing, over the floodplain close to the walls. 'Deep flows' ($r_h < 2$) are characterized by a very weak shear in the transition region. The wall boundary layer increases in size and more and stronger macrovortices are generated over the floodplains, while the influence of the topography is much weaker.

3. Fundamentals of mixing

The most natural framework for analysing mixing processes is the Lagrangian (or material) viewpoint, which studies what happens to material particles during the flow motion. Given an Eulerian velocity field, it is possible to obtain trajectories of material particles by integrating the following equation:

$$\frac{\mathrm{d}\boldsymbol{x}^*(t^*)}{\mathrm{d}t^*} = \boldsymbol{u}^*(\boldsymbol{x}^*, t^*), \tag{3.1}$$

where $\boldsymbol{x}^*(t^*)$ is the particle position at time t^* and $\boldsymbol{u}^*(\boldsymbol{x}^*, t^*)$ is the Eulerian velocity at point $\boldsymbol{x}^*$ and time t^*. We calculated particle trajectories using a fourth-order Runge–Kutta algorithm with adaptive step size, which has a local accuracy of order $(\Delta t^*)^4$, where Δt^* is the integration time step. In more detail, for each flow field, we inseminated the experimental flow with approximately $O(10^4)$ 'numerical particles' (massless) on a regular grid (of constant size Δx^* and Δy^*) and, subsequently, evaluated the tracers' trajectories by integrating (3.1) in time with the above Runge–Kutta algorithm employing a bi-cubic spatial interpolation and a polynomial time interpolation of the experimental Eulerian fields. This approach, namely to calculate numerically the particle trajectories starting from measured Eulerian fields, is commonly adopted in mixing studies (Lekien *et al.* 2005).

To test whether the particle trajectories reach quasi-stationary conditions, we have computed the mean Lagrangian kinetic energy $E_L^*(t^*) = (1/2)\langle u_L^{*'}(x^*, y^*, t^*)^2 + v_L^{*'}(x^*, y^*, t^*)^2\rangle$, where $u_L^{*'}$ and $v_L^{*'}$ are the Lagrangian velocity fluctuations and the angle brackets indicate average over the total number of particles. The Lagrangian kinetic energy together with its Eulerian (E_E^*) counterpart is illustrated for sample shallow and deep flow conditions in figure 3. From an inspection of figure 3 it is clear that E_L^* and E_E^* attain very close values, which are also almost constant over the entire duration of the experiments, and residual fluctuations are due to low-frequency turbulent events.

Of the different Eulerian techniques used to characterize dispersion phenomena, we have tested the Okubo–Weiss criterion (Okubo 1970; Weiss 1991) and its generalization to time-dependent flows (Hua & Kline 1998). These criteria enable both the partitioning of the flow into regions with different dynamical properties and the characterization of flows with a complex topology. By quantifying the local rate of separation of initially close trajectories, an attempt is also made to relate the nature of the stirring processes to the local topology of the flow. For steady flows, characterized by velocity gradients which are also slowly varying in space, the

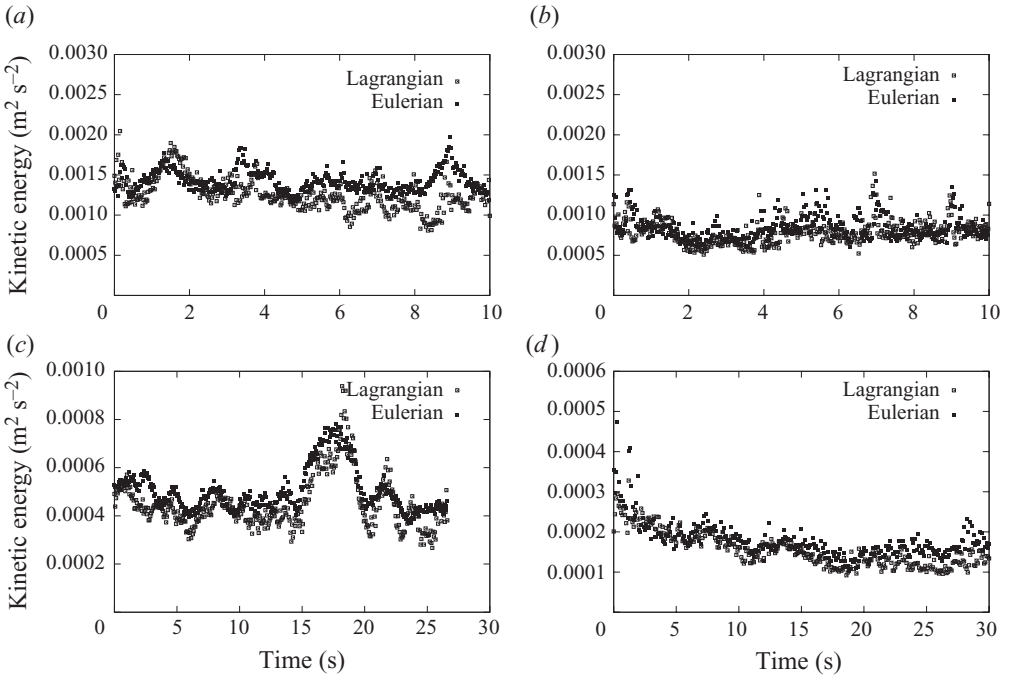

FIGURE 3. Eulerian and Lagrangian kinetic energy (respectively E_E^* and E_L^*) for (a, c) shallow flows (EXP101 and EXP201, respectively) and (b, d) deep flows (EXP213 and EXP112, respectively).

Okubo–Weiss criterion makes use of the eigenvalue of the local velocity gradient tensor $\boldsymbol{D}^*$. The tensor $\boldsymbol{D}^*$ is such that, for incompressible fluid, $\boldsymbol{D}^{*2} = \lambda_0^* \boldsymbol{I}$, where $\lambda_0^* = -\det(\boldsymbol{D}^*)$ is the product of the eigenvalue of the velocity gradient tensor. The Okubo–Weiss criterion consists of the evaluation of λ_0^*, which can also be written as (Weiss 1991)

$$\lambda_0^* = \tfrac{1}{4}(S^{*2} - \omega^{*2}), \tag{3.2}$$

where $S^{*2} = S_n^{*2} + S_s^{*2}$ is the total square strain, sum of the normal (S_n^*) and shear (S_s^*) components, and ω^{*2} is the square vorticity, which in an (x^*, y^*), 2D flow has only the out-of-plane component ω_z^{*2}. Depending on the sign of λ_0^*, the flow has different local properties. The largest dispersion occurs in flow regions where $\lambda_0^* > 0$, where the flow can be taken as locally hyperbolic (strain overcomes rotation); on the other hand, where $\lambda_0^* < 0$, the flow is dominated by rotation, and it is assumed as locally elliptical. Hyperbolic regions, which act as fluid jets, are characterized by a local exponential divergence of nearby particles; on the contrary, elliptical regions are characterized by an approximately constant distance between adjacent particles.

For time-dependent flows, Hua & Kline (1998) proposed an extension of the Okubo–Weiss criterion that requires the computation of the eigenvalues of the local acceleration tensor, which can be written as $\boldsymbol{N}^* = \lambda_0^* \boldsymbol{I} + \mathrm{d}\boldsymbol{D}^*/\mathrm{d}t^*$. The Hua–Kline criterion is, then, based on the sign of the largest eigenvalue of $\boldsymbol{N}^*$, namely $\lambda_+^* = \lambda_0^* + \lambda_1^*$, where

$$\lambda_1^* = \sqrt{\left(\frac{\partial S^*}{\partial t^*}\right)^2 - \left(\frac{\partial \omega^*}{\partial t^*}\right)^2}. \tag{3.3}$$

Both the above criteria provide a description of the flow in terms of stable elliptical regions and unstable hyperbolic regions, but the latter is closer to a pure Lagrangian point of view (Boffetta *et al.* 2001). Note that neither the Okubo–Weiss eigenvalue nor the Hua–Kline eigenvalue identifies Lagrangian material structures, since they are strictly valid only locally. The identification of the Lagrangian coherent structures (Wiggins 2005) is beyond the scope of the present work. We simply use λ_0^* and λ_+^* to describe qualitatively the dynamics of different flow regions (e.g. vortices and high-strain regions).

Lagrangian measures of mixing can be used as based on either single-particle or multiple-particle statistics. In the following, a brief description of these statistics will be provided.

3.1. *Single-particle statistics*

Once the particle trajectories are known, the absolute dispersion tensor, $\boldsymbol{A}^{*(2)}$, can be found (see Provenzale 1999, among others)

$$A_{ij}^{*(2)}(t^*, t_0^*) = \frac{1}{M}\sum_{m=1}^{M}\left\{\left[x_i^{*m}(t^*) - x_i^{*m}(t_0^*)\right]\left[x_j^{*m}(t^*) - x_j^{*m}(t_0^*)\right]\right\}, \tag{3.4}$$

where M is the total number of particles, $\boldsymbol{x}^{*m}(t^*)$ is the position of the mth particle at time t^* and $\boldsymbol{x}^{*m}(t_0^*)$ is its initial position (at time t_0^*). If the flow is isotropic, $\boldsymbol{A}^{*(2)}$ is a multiple of the identity matrix. The mean-square displacement is given by the trace of $\boldsymbol{A}^{*(2)}$, defined as total absolute dispersion, which reads

$$a^{*2} = \mathrm{Tr}\left(\boldsymbol{A}^{*(2)}\right). \tag{3.5}$$

However, in the most general non-isotropic case, the average square displacements along the x^*- and y^*-directions may be different owing to flow anisotropy. The time derivatives of absolute dispersion, defined as absolute $K^{*(1)}$ diffusivity, can be written as

$$K^{*(1)} = \frac{1}{2}\frac{\mathrm{d}}{\mathrm{d}t^*}\left[\mathrm{Tr}\left(\boldsymbol{A}^{*(2)}\right)\right]. \tag{3.6}$$

The absolute diffusivity coefficient measures the average rate of spreading of the particles in the domain.

The time dependence of the diffusivity coefficients enables us to clearly identify different dispersion regimes (Provenzale 1999; Boffetta *et al.* 2001): in a wide variety of applications, the absolute dispersion obeys power laws of the type $a^{*2}(t^*, t_0^*) \sim t^{*\gamma}$ and, therefore, the absolute diffusivity can be described as $K^{*(1)} \sim t^{*\gamma-1}$. The fundamental results obtained by Taylor (1921) in the case of homogeneous turbulence show that, for short times after particles' deployment, an exponent $\gamma = 2$ can be expected, describing the so-called ballistic regime. For times longer than an integral time scale T_L^*, defined as the decorrelation time, the exponent should be $\gamma = 1$, the so-called diffusive or Brownian regime. The Lagrangian time scale T_L^* is evaluated as the integral of the normalized velocity autocorrelation $\mathscr{R}(\tau)$:

$$T_L^* = \int_0^\infty \mathscr{R}(\tau^*)\,\mathrm{d}\tau^*. \tag{3.7}$$

For intermediate times, a variety of scalings have been found, depending on the specific flow under investigation. The asymptotic Taylor regimes have been extended by Babiano *et al.* (1987), who showed that the exponent of the time power laws of the absolute dispersion depends on the slope of the Lagrangian energy spectrum in the

frequency domain ($L^*(\sigma^*)$). In addition, they have proved that the Brownian regime is independent of the restrictive hypothesis of flow homogeneity. This result is supported by Lagrangian data derived from inhomogeneous oceanic and atmospheric velocity fields; see Elhmaïdi, Provenzale & Babiano (1993) and references cited therein. It is easy to show that the absolute diffusivity $K^{*(1)}$ can be expressed in terms of the normalized velocity autocorrelation $\mathscr{R}(\tau^*)$ (see LaCasce 2008, among others):

$$K^{*(1)} = \nu^{*2} \int_0^\infty \mathscr{R}(\tau^*)\,\mathrm{d}\tau^* = \nu^{*2} T_L^*. \tag{3.8}$$

The diffusivity is, thus, the product of the velocity variance (ν^{*2}) and the Lagrangian time scale. If we now write the Lagrangian frequency spectrum $L^*(\sigma^*)$ by using the Fourier transform of the velocity autocorrelation as

$$L^*(\sigma^*) = 2\nu^{*2} \int_0^\infty \mathscr{R}(\tau^*)\cos(2\pi\sigma^*\tau^*)\,\mathrm{d}\tau^*, \tag{3.9}$$

we find that for $\sigma^* = 0$, the spectrum is proportional to the absolute diffusivity:

$$L^*(0) = 2\nu^{*2} \int_0^\infty \mathscr{R}(\tau^*)\,\mathrm{d}\tau^* = 2\nu^{*2} T_L^* = 2K^{*(1)}. \tag{3.10}$$

The latter result implies that the absolute diffusivity is determined by the lowest-frequency motion, e.g. by the mean flow (Davis 1982). Indeed, a constant mean causes the absolute dispersion to increase quadratically in time, and thus the diffusivity to increase linearly in time. In the case of compound channel flows, a mean motion does exist in the streamwise direction and it is non-homogeneous over the cross-section. The mean streamwise velocity assumes a bell-like distribution as shown in Stocchino & Brocchini (2010) and its shape depends strongly on the flow depth ratio r_h. It is, therefore, necessary to remove the mean flow prior to evaluating the absolute statistics. This issue has also been rigorously studied by Davis in connection with ocean dynamics (Davis 1982, 1983). The general idea is to subtract the ensemble-averaged Eulerian velocity from the actual velocity, while retaining where necessary, the spatial dependence of the average. For a 2D flow evolving in the (x^*, y^*)-plane, the residual velocity field reads as

$$\boldsymbol{u}^{*\prime}(x^*, y^*, t^*) = \boldsymbol{u}^*(x^*, y^*, t^*) - \boldsymbol{U}^*(x^*, y^*), \tag{3.11}$$

where $\boldsymbol{U}^*(x^*, y^*)$ indicates the velocity averaged over the duration of the single realization. This method is adequate to handle flows that are inhomogeneous, like in the present case or in oceanographic applications, while the classical results of Taylor were obtained assuming $\boldsymbol{U}^*(x^*, y^*) = 0$, i.e. for homogeneous flows. The absolute statistics are then derived from the residual velocities.

3.2. *Multiple-particles statistics*

The relative dispersion can be defined as the mean-square distance at time t^* between a pair of particles that at time t_0^* have a distance equal to d_0^*, and is formulated as

$$R_{ij}^{*(2)}(t^*, t_0^*, d_0^*) = \frac{1}{M-1} \sum_{m=1}^{M-1} \left\{ \left[x_i^{*m}(t^*) - x_i^{*m+1}(t^*) \right] \left[x_j^{*m}(t^*) - x_j^{*m+1}(t^*) \right] \right\}, \tag{3.12}$$

where $(M-1)$ is the number of particle pairs. In analogy with the absolute statistics, a total relative dispersion, mean-square relative displacement between pairs, can be

defined as the trace of the matrix given by (3.12):

$$r^{*2} = \mathrm{Tr}\left(\boldsymbol{R}^{*(2)}\right). \tag{3.13}$$

The time derivative of relative dispersion, defined as the relative diffusivity $K^{*(2)}$, can be written as

$$K^{*(2)} = \frac{1}{2}\frac{\mathrm{d}}{\mathrm{d}t^*}\left[\mathrm{Tr}\left(\boldsymbol{R}^{*(2)}\right)\right]. \tag{3.14}$$

Classical studies on 2D turbulence (Kraichnan 1966; Lin 1972; Bennett 1984; Babiano *et al.* 1990) demonstrate that the two distinct cascading regimes (inverse energy cascade and direct enstrophy cascade) can be characterized in terms of relative diffusivity: $K^{(2)} \propto r^{4/3}$ in the energy cascade and $K^{(2)} \propto r^2$ in the enstrophy cascade. The former relationship (the 'Richardson–Obukhov law') derives from a cubic growth with time of the mean-squared relative displacement r^2, while the latter Kraichnan–Lin law corresponds to an exponential growth in time of r^2. Bennett (1984) showed that the dependence of the diffusivity on separation directly reflects the slope of the energy spectrum in the wavenumber space $E(k) \propto k^{-\alpha}$, linking the inverse energy cascade ($\alpha = 5/3$) to a growth of relative diffusivity proportional to $r^{4/3}$ and the enstrophy cascade ($\alpha = 3$) to a growth proportional to r^2.

As pointed out by Er-El & Peskin (1981), the two-particle diffusion in 2D turbulence can be controlled by two distinct dynamical mechanisms leading to two different regimes known as 'local dispersion' and 'non-local dispersion'. In local dynamics, the relative dispersion is controlled by a local straining mechanism which is not really effective in causing further separation of the particles, while in the case of non-local dynamics particles are subjected to very strong shear produced by the large-scale structures. Both dispersion regimes can be identified on the basis of the value of the energy spectrum slope α (Bennett 1984). The local dynamics is characterized by $1 < \alpha < 3$ and the dispersion of pairs is dominated by eddies of the same scale of their separation. Hence, the corresponding diffusivity scales as

$$K^{(2)} \equiv \frac{1}{2}\frac{\mathrm{d}}{\mathrm{d}t}r^2 \propto r^{(\alpha+1)/2}. \tag{3.15}$$

Non-local dynamics, otherwise, is characterized by values of α larger than 3 (steeper spectra).

Valuable additional information on the dispersion regimes can be obtained from the analysis of the p.d.f.s of the separations of pairs of particles. The p.d.f., a normalized histogram, of displacements is crucial for the estimate of the flow and mixing regimes because all moments are derived from it: the spread about the centre of mass can be measured by the variance of the displacements, i.e. using the second-order moment (LaCasce 2008). Usually, the dispersion measures the width of the p.d.f. but it does not give any information on the shape of the distribution. To get a more detailed description of the p.d.f.s, it is necessary to evaluate higher-order moments; in particular the fourth-order moment, the kurtosis *ku*, provides important insight into the shape of the distribution. Particles undergoing a random walk lead to a Gaussian p.d.f., characterized by a kurtosis *ku* of 3. More often, a coherent advection produces p.d.f.s which are not Gaussian and characterized by larger values of the kurtosis. As suggested by Er-El & Peskin (1981), Bennett (1984) and LaCasce (2008), under local dispersion the separation kurtosis is constant in time, while for non-local dynamics it grows exponentially.

Finally, a potential difficulty in the use of the relative dispersion as a suitable measure concerns the methods of averaging distances at fixed times. If the dispersion

is dominated by flow structures with size comparable with the particles' separation, averaging pairs with different separations may blur the dependences. The FSLEs, consisting of averages of times at fixed distances, provide a useful alternative approach. In comparison with the relative diffusivity, the FSLE has the additional advantage of being an integral quantity rather than a derivative, and generally, it tends to be smoother than the diffusivity and less sensitive to random errors, which always affect experimental measurements. To calculate the FSLE, it is necessary to first choose a set of distances that increase recursively,

$$r_n^* = \alpha r_{n-1}^* = \alpha^n r_0^*, \tag{3.16}$$

where α is an arbitrary constant larger than unity, and then calculate the times required (known as 'exit time' T_n^*) for each pair displacement to grow to the successive r_n^*. The estimate for the maximum Lyapunov exponent varies with distance and reads as

$$\lambda_s^*(n) = \frac{1}{\log(\alpha)} \left\langle \frac{1}{T_n^*} \right\rangle. \tag{3.17}$$

If the dispersion has a power-law dependence with time, like for local dispersion, the FSLEs exhibit a power-law dependence on the separation. In particular, as the dispersion is proportional to a power of time as ($r^2 \propto t^\gamma$), the FSLEs, being mean inverse times, scale like $\lambda_S \propto r^{-2/\gamma}$. Generally, results obtained by means of the FSLE should recall those obtained by means of the relative diffusivity.

4. Results of the mixing processes

4.1. *Experimental observations of Eulerian flow fields*

We first analyse the measured two-dimensional Eulerian velocity fields with the aim of distinguishing regions with different dynamical properties, using the value and, more importantly, the sign of the eigenvalue λ_+^*, as suggested by Hua & Kline (1998). An example of the computed values of λ_+^* is shown in figure 4(*a–c*) in the case of shallow flow, intermediate flow and deep flow conditions, respectively. Similar results have been obtained using the Okubo–Weiss criterion based on the evaluation of the eigenvalue λ_0^*: the unsteady eigenvalue λ_1^* has been found to be always at least one order of magnitude smaller than λ_0^*. This suggests, as expected, that the flow under investigation is slowly varying in time.

In the case of shallow conditions, the flow fields are dominated by large-scale 2D coherent structures identified by large patches of negative λ_+^*, with a surrounding turbulent field characterized mainly by a low-intensity, positive eigenvalue. Among nearby vortical structures, intense hyperbolic regions are clearly visible. The macrovortices are observed at the transition region (indicated by the dash-dotted white lines in figure 4) where the flow depth jump is localized. The vortex generation mechanism was discussed in detail by Soldini *et al.* (2004). Fundamental results of the study are that the size of the macrovortices scales with the downstream distance over which velocity fronts cross the depth jump and that the intensity of the macrovortices depends on the depth jump itself. In their recent experimental work, Stocchino & Brocchini (2010) observed that the size of the macrovortices scales well with that of the transition region and that these coherent structures remain confined within the transition regions while they are convected downstream by the mean flow. The quasi-2D macrovortices behave as organized domains with a distinct dynamical role. On the contrary, for lower values of the flow depth ratio r_h, corresponding to intermediate flow conditions, the Hua–Kline eigenvalue is more randomly distributed

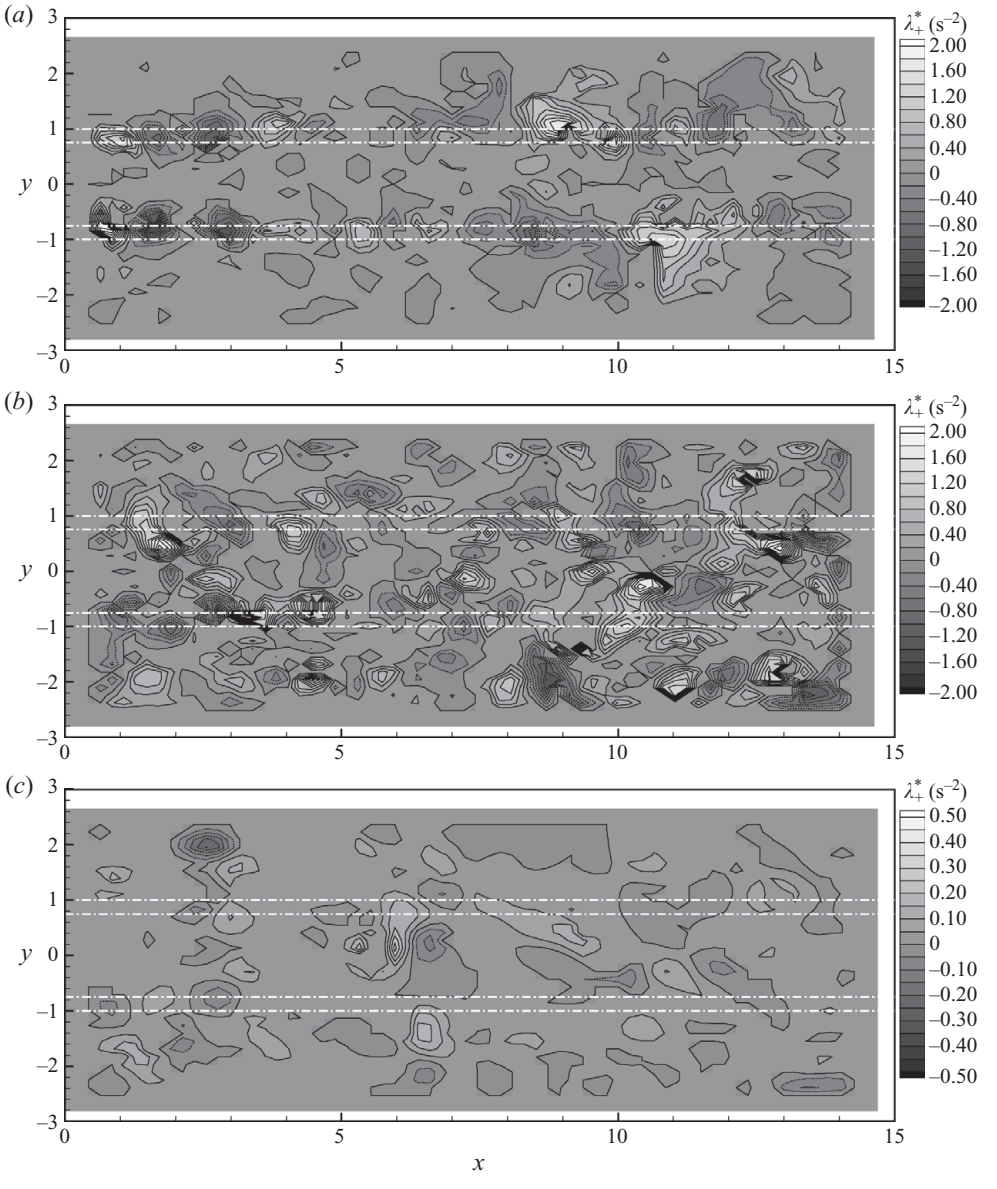

FIGURE 4. Examples of 2D maps of the positive Hua–Kline eigenvalue λ_+^*: (*a*) shallow flow conditions (EXP201, $r_h = 4.16$, $Fr = 0.60$), (*b*) intermediate flow conditions (EXP205, $r_h = 2.04$, $Fr = 0.76$) and (*c*) deep flow conditions (EXP112, $r_h = 1.28$, $Fr = 0.142$). The dotted white lines indicate the transition regions of the compound channel. For the deep flow, the contour range has been reduced.

in the domain and fewer macrovortices can be recognized, located either in the transition regions or in the floodplains. The background turbulent field is, in this case, characterized by a distribution of λ_+^* oscillating between moderate positive and negative values. Decreasing further r_h, i.e. moving to deeper flow conditions, the distribution of the Hua–Kline eigenvalue is even more uniform and less intense than in the previous case (the range of the contour levels has been reduced to improve the

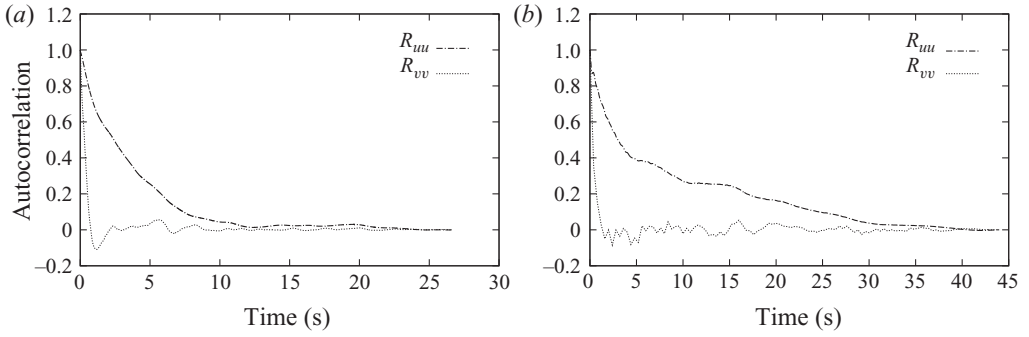

FIGURE 5. Autocorrelation for (*a*) shallow flows (EXP201) and (*b*) deep flows (EXP112).

plot quality). The non-organized background turbulence occupies most of the flow domain and dominates the dynamics.

4.2. *Absolute statistics*

We start the study of the Lagrangian mixing with the analysis of single-particle or absolute statistics evaluated from the numerical trajectories, see (3.4) and (3.6), respectively.

We have first evaluated the Lagrangian integral time scales T^*_{uL} and T^*_{vL}, using the procedures described in Guala *et al.* (2007) and Luo *et al.* (2007), for each experiment and for both the Lagrangian residual components $u^{*'}_L$ and $v^{*'}_L$. Therefore, the normalized Lagrangian autocorrelation of the ith velocity component has been computed using the following estimator:

$$\mathscr{R}_{ii}(\tau^*) = \frac{\dfrac{1}{M}\displaystyle\sum_{M} \rho^*_{L_{ii}}(\tau^*)}{[\mathrm{Var}(u^{*'}_{Li})\mathrm{Var}(u^{*'}_{Li})]^{1/2}}, \tag{4.1}$$

where $\rho^*_{L_{ii}}(\tau^*)$ is the covariance of the velocity component along the ith direction, which is defined as

$$\rho^*_{L_{ii}}(\tau^*) = \langle u^{*'}_{Li}(t^*) u^{*'}_{Li}(t^* + \tau^*) \rangle. \tag{4.2}$$

Here, the angle brackets indicate an average over the entire duration of each trajectory, whereas the covariance is averaged over the set of the N trajectories appearing in (4.1). The covariance is then normalized with the variance of the velocity component $\mathrm{Var}(u^{*'}_{Li})$.

Typical examples of the normalized Lagrangian autocorrelation function for the streamwise $\mathscr{R}_{uu}(\tau^*)$ and spanwise $\mathscr{R}_{vv}(\tau^*)$ directions are shown in figure 5 for one sample shallow flow and one sample deep flow. Clearly, the spanwise autocorrelation decays more rapidly than the streamwise autocorrelation, leading to a much smaller Lagrangian integral scale, thus highlighting the fact that quasi-uniform flows in compound channels are fundamentally unidirectional. Moreover, the results of the cross-stream correlation for the shallow flow show a clear initial dip, indicating the presence of trapping vortices, while the results for the deep flow condition display a correlation with a lower energy and a noisy shape. Such a result suggests that shallow flows are dominated by macrovortices, while deep flows are mainly shear-dominated flows. Starting from the Lagrangian time integral scales, the corresponding spatial integral scales (L^*_{uL}, L^*_{vL}) can be easily computed. The computed values of the Lagrangian time scales for all the experiments are listed in table 2, together

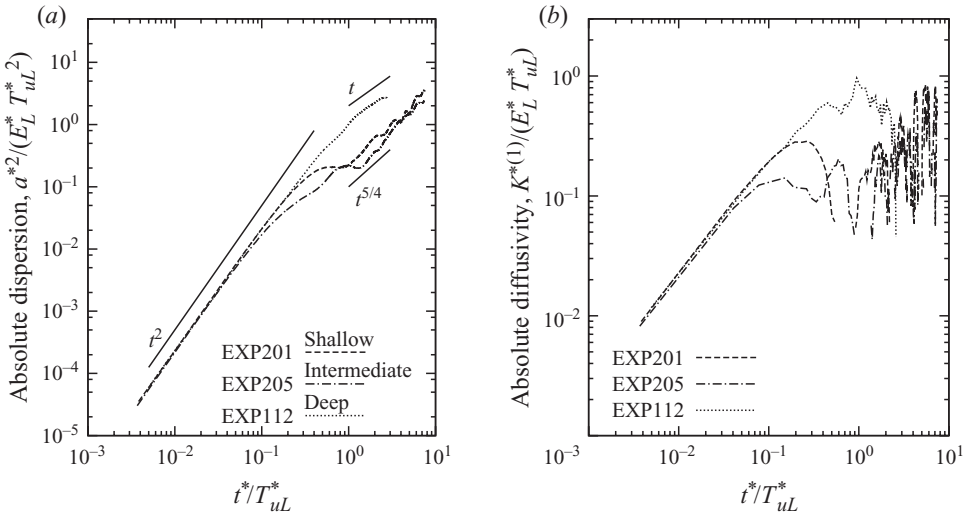

FIGURE 6. (*a*) Absolute dispersion and (*b*) absolute diffusivity. EXP201: $Fr = 0.6$, $r_h = 4.16$; EXP205: $Fr = 0.69$, $r_h = 5.57$; EXP112: $Fr = 0.14$, $r_h = 1.28$.

with values of the Eulerian integral scales (T_{uE}^*, T_{vE}^*), which have been calculated as the time integrals of the normalized Eulerian autocorrelation functions (the Eulerian integral scales are always greater than the Lagrangian scales).

In the following, the results are given in dimensionless form (unstarred variables) using the quantities defined above (T_{uL}^*, L_{uL}^*) together with the time-averaged Lagrangian kinetic energy E_L^* to make dimensionless the absolute dispersion and diffusivity.

The dimensionless absolute dispersion a^2 is a function of time as shown by the sample cases (shallow flow of EXP201, intermediate flow of EXP205 and deep flow of EXP112) illustrated in figure 6(*a*). The first significant difference between the flow regimes is that a^2 shows a non-monotonic behaviour in the shallow flow conditions (see range $0.2 \leqslant t^*/T_{uL}^* \leqslant 2$), whereas it monotonically increases with time in the deep flow experiment. A similar behaviour has been described in Elhmaïdi *et al.* (1993), where the single-particle dispersion has been studied by purely 2D numerical simulations characterized by few long-lived, large-scale vortices immersed in an almost homogeneous turbulent background. In that case, the authors justified the non-monotonic trend of a^2 by the influence of the macrovortices on the flow mixing. In particular, they analysed two different initial conditions: (i) a uniform seeding over the entire domain and (ii) a seeding localized in the vicinity of an isolated vortex. The latter initial condition led to the non-monotonic behaviour, whereas the dispersion observed in the case of uniform seeding was mainly forced by the background turbulence rather than by the macrovortices, which occupied a small portion of the entire domain.

It is interesting to note that for the shallow flows, the absolute dispersion is a non-monotonic function of time even if we seeded the domain with an initial homogeneous distribution of particles. This suggests that for the present class of flows, the dominant dynamical features are the transitional macrovortices, which control the overall dispersive process. On the contrary, such vortical structures are almost absent in the case of deep flows with a consequent smoother dispersive process. If we now analyse in detail the results shown in figure 6, the single-particle dispersion

Experiment	r_h (−)	Fr (−)	E_L^* (m^2 s^{-2})	T_{uL}^* (s)	T_{vL}^* (s)	L_{uL}^* (m)	L_{vL}^* (m)	E_E^* (m^2 s^{-2})	T_{uE}^* (s)	T_{vE}^* (s)	T_T (−)
					Shallow flows						
EXP101	3.69	0.88	0.001126	4.0206	0.4421	0.1349	0.0148	0.001427	4.1507	0.4904	0.0950
EXP102	3.23	0.91	0.001364	3.8013	0.3188	0.1404	0.0118	0.001699	3.9274	0.4190	0.1090
EXP04	3.69	0.87	0.001316	1.2488	0.1684	0.0453	0.0061	0.001414	4.1766	0.2690	0.2908
EXP06.1	3.10	0.92	0.001241	1.2396	0.1465	0.0437	0.0052	0.001401	4.0331	0.1585	0.3257
EXP010	4.42	0.73	0.000943	1.2340	0.2160	0.0379	0.0066	0.001019	4.3962	0.6238	0.2767
EXP011	3.50	0.77	0.001438	0.8759	0.1901	0.0332	0.0072	0.001656	4.0856	0.3379	0.3910
EXP012	3.40	0.80	0.001264	1.3119	0.1995	0.0466	0.0071	0.002280	4.0648	0.4022	0.2113
EXP201	4.16	0.60	0.000399	3.4787	0.3684	0.0694	0.0074	0.000504	11.0929	1.4211	0.1737
EXP202	3.60	0.62	0.000409	3.1638	0.3600	0.0640	0.0073	0.000549	10.8788	1.3098	0.2005
EXP203	3.36	0.64	0.000440	3.3460	0.4185	0.0702	0.0088	0.000529	10.8231	1.1654	0.1948
EXP204	3.08	0.65	0.000458	3.1524	0.4492	0.0675	0.0096	0.000584	10.5168	1.2757	0.2163
EXP001	3.69	0.44	0.000202	1.5931	0.7407	0.0226	0.0105	0.000241	8.2112	0.9079	0.6346
EXP002	3.43	0.46	0.000091	2.0198	0.9157	0.0192	0.0087	0.000079	9.1400	1.8571	0.4587
EXP003	3.05	0.47	0.000090	2.8517	0.7300	0.0271	0.0069	0.000076	9.0556	1.3710	0.3272
					Intermediate flows						
EXP103	2.62	0.97	0.000505	4.3555	0.5117	0.0979	0.0115	0.000598	4.4370	0.5327	0.0944
EXP104	2.29	1.03	0.000435	4.2171	0.8945	0.0880	0.0187	0.000533	4.2865	0.7623	0.1082
EXP105	2.15	1.05	0.000504	4.0335	0.8769	0.0906	0.0197	0.000621	4.1102	0.5530	0.1186
EXP106	2.07	1.07	0.000631	3.0521	0.6168	0.0767	0.0155	0.000757	3.1571	0.4383	0.1418
EXP107	2.03	1.07	0.000624	2.9748	0.6405	0.0743	0.0160	0.000761	3.1010	0.4217	0.1487
EXP06.6	2.92	0.94	0.000975	1.4206	0.1014	0.0444	0.0032	0.001045	4.1898	0.1399	0.2883
EXP07	2.71	0.96	0.000627	1.8842	0.1332	0.0472	0.0033	0.000639	4.4087	0.1899	0.2146
EXP10	2.32	1.02	0.000481	1.7625	0.3171	0.0386	0.0070	0.000968	4.3356	0.5746	0.2590
EXP12	2.11	1.06	0.000496	1.6093	0.4772	0.0358	0.0106	0.000619	3.2908	0.3588	0.2628
EXP13	2.02	1.07	0.000668	1.5634	0.5063	0.0404	0.0131	0.001302	3.0648	0.3298	0.2606
EXP013	2.36	0.84	0.000347	2.4633	0.2385	0.0459	0.0044	0.000436	4.5913	1.0029	0.1506
EXP014	2.30	0.87	0.000409	1.6821	0.2518	0.0340	0.0051	0.000417	3.0060	0.6953	0.2161
EXP015	2.10	0.92	0.000727	1.3271	0.2075	0.0358	0.0056	0.000738	2.6511	0.6265	0.2850

TABLE 2. Relevant Lagrangian and Eulerian integral quantities of the whole set of experiments.

Experiment	r_h (−)	Fr (−)	E_L^* (m^2 s^{-2})	T_{uL}^* (s)	T_{vL}^* (s)	L_{uL}^* (m)	L_{vL}^* (m)	E_E^* (m^2 s^{-2})	T_{uE}^* (s)	T_{vE}^* (s)	T_T (−)
EXP205	2.57	0.69	0.000367	3.6030	0.3118	0.0691	0.0060	0.000417	10.8472	1.3190	0.1949
EXP206	2.40	0.71	0.000321	3.0163	0.2016	0.0541	0.0036	0.000377	5.6998	0.9195	0.2230
EXP207	2.26	0.73	0.000326	2.6958	0.2093	0.0487	0.0038	0.000392	4.2514	0.6814	0.2433
EXP208	2.16	0.74	0.000340	2.6557	0.2684	0.0489	0.0049	0.000399	4.1548	0.5984	0.2496
EXP209	2.04	0.76	0.000361	2.5942	0.1990	0.0493	0.0038	0.000437	4.1062	0.6083	0.2552
EXP004	2.61	0.50	0.000112	2.4703	0.3950	0.0261	0.0042	0.000099	4.3513	0.2518	0.3325
EXP005	2.40	0.51	0.000106	2.3586	0.2538	0.0242	0.0026	0.000091	4.1502	0.3021	0.3387
EXP006	2.20	0.53	0.000119	2.0601	0.2515	0.0225	0.0027	0.000117	3.7111	0.2777	0.3995
					Deep flows						
EXP108	1.95	1.09	0.000742	2.8216	0.5657	0.0769	0.0154	0.000900	2.9520	0.3239	0.1591
EXP109	1.86	1.11	0.000764	2.5225	0.5872	0.0697	0.0162	0.000957	2.7497	0.2755	0.1759
EXP110	1.82	1.12	0.000818	2.4143	0.4879	0.0691	0.0140	0.001028	2.6479	0.2394	0.1848
EXP112	1.28	0.14	0.000128	8.0753	0.3181	0.0913	0.0036	0.000179	12.5836	0.7280	0.1220
EXP14	1.96	1.09	0.000695	1.4211	0.4231	0.0375	0.0112	0.000793	3.0008	0.2512	0.3005
EXP16	1.85	1.15	0.000912	1.4239	0.4231	0.0430	0.0128	0.002154	2.6424	0.2549	0.2644
EXP17	1.82	1.13	0.000783	1.2175	0.5089	0.0341	0.0142	0.000931	2.6143	0.2634	0.3558
EXP017	1.85	0.96	0.001136	1.0174	0.1556	0.0343	0.0052	0.001226	2.4007	0.3511	0.3331
EXP018	1.82	0.99	0.001548	1.0888	0.1254	0.0428	0.0049	0.001954	2.2659	0.3117	0.3155
EXP210	1.89	0.78	0.000471	2.5864	0.2111	0.0561	0.0046	0.000568	3.8975	0.5730	0.2534
EXP211	1.83	0.79	0.000510	2.6535	0.1903	0.0599	0.0043	0.000606	3.8099	0.3809	0.2451
EXP212	1.73	0.81	0.000599	2.5977	0.2091	0.0636	0.0051	0.000716	3.6902	0.4447	0.2454
EXP213	1.68	0.82	0.000679	2.4911	0.2051	0.0649	0.0053	0.000828	3.5203	0.2990	0.2555
EXP007	1.97	0.55	0.000172	1.9276	0.1437	0.0253	0.0019	0.000172	3.6659	0.2271	0.3799
EXP008	1.83	0.56	0.000263	1.5502	0.0985	0.0251	0.0016	0.000406	3.0661	0.1658	0.4369
EXP009	1.77	0.57	0.000319	1.7301	0.1325	0.0309	0.0024	0.000801	2.6982	0.1471	0.2556

TABLE 2. Continued.

of EXP201 is seen to be characterized by different regimes. An initial ballistic regime is observed until a^2 reaches a local maximum at a value that is related to the typical size of the macrovortices: for the specific case shown, $a^2 \simeq 0.2$ corresponds to a length of about $\sqrt{a^2} = 0.45$. This compares fairly well with the dimensionless transition region ($L_i = W^*_{tr}/L^*_{uL} = 0.36$) which, recalling the studies of Soldini *et al.* (2004) and Stocchino & Brocchini (2010) summarized at the beginning of § 4, provides a suitable scale for the macrovortices. In view of this and of some results which follow, we regard this scale as the 'injection scale' $L_i = W_{tr}$ for the turbulence energy. Moreover, the time for which the local maximum of the absolute dispersion occurs is of the same order of magnitude as the vortex turnover time ($\sim 3T_T$), defined as $T_T = 1/\sqrt{2Z^2}$, where Z^2 is the total enstrophy (calculated as the ensemble-averaged square vorticity, $Z^2 = \langle ||\boldsymbol{\omega}||^2 \rangle / 2$). In table 2, the values of the dimensionless turnover time are reported for all the experiments, where the turnover time has been made dimensionless with the Lagrangian integral time scale. It is possible to evaluate a dimensionless turnover length scale (L_T) associated with T_T. A simple inspection of the available data shows that $1.5 \leqslant L_i/L_T \leqslant 3.5$. The absolute dispersion attains such a local maximum as soon as the particles trapped in coherent vortical structures undergo almost regular oscillation on a length scale comparable with the vortex diameter.

For longer times, particles are influenced by the straining regions that surround the large-scale structures and the absolute dispersion increases with time following a power law with an exponent closer to 5/4, as also described in Elhmaïdi *et al.* (1993). Finally, after such an intermediate regime, a^2 grows with t following a dependence which resembles that of a Brownian regime ($a^2 \propto t$). At this stage, the influence of the macrovortices is less vigorous and the background turbulence dominates the mixing.

Decreasing the flow depth ratio r_h, as shown by Stocchino & Brocchini (2010), the intermediate flows are characterized by the simultaneous generation of macrovortices both at the transition region and at the sidewalls. In this case, transitional macrovortices still strongly influence the growth of the absolute dispersion a^2, leading to a close similarity with the shallow flows as shown in figure 6 (EXP205).

Decreasing further r_h, we reach the deep flows. In this case, the behaviour of the single-particle dispersion is mainly monotonic with no evidence of oscillations in the intermediate regime, as observed for the shallow and intermediate flows. The Brownian regime is clearly attained after a time of about $(1.3\text{–}1.5)T^*_{uL}$, especially in the case of EXP112, characterized by very deep conditions ($r_h = 1.2$). The absence of transitional coherent vortices in deep flows leads to a more regular transition from the initial ballistic regime towards a fully developed Brownian regime.

Given the behaviour of the absolute dispersion shown in figure 6(a), the corresponding absolute diffusivity $K^{(1)}$, i.e. the time derivative of a^2, shown in figure 6(b) is, not surprisingly, rather irregular except for the initial ballistic regimes. This is a direct consequence of the non-monotonic behaviour of a^2. However, for large times the absolute diffusivity seems to oscillate with an almost-constant upper bound, resembling what would occur in the case of an equilibrium regime.

Finally, we have evaluated the anisotropy of the absolute statistics by computing separately $A^{(2)}_x$, $A^{(2)}_y$, $K^{(1)}_x$ and $K^{(1)}_y$, which are respectively the contributions to the total absolute dispersion and diffusivity in the x- and y-directions (see figure 7). In the case of shallow flows (EXP201, figure 7a,b), the dispersions in the streamwise and spanwise directions are fairly close, indicating a weak anisotropy. In this class of flows, dominated by large-scale vortices, the contribution of the coherent structures produces an intense dispersion in both directions, especially for long times. On the contrary, the few macrovortices that characterize the deep flows (EXP112, figure 7c,d)

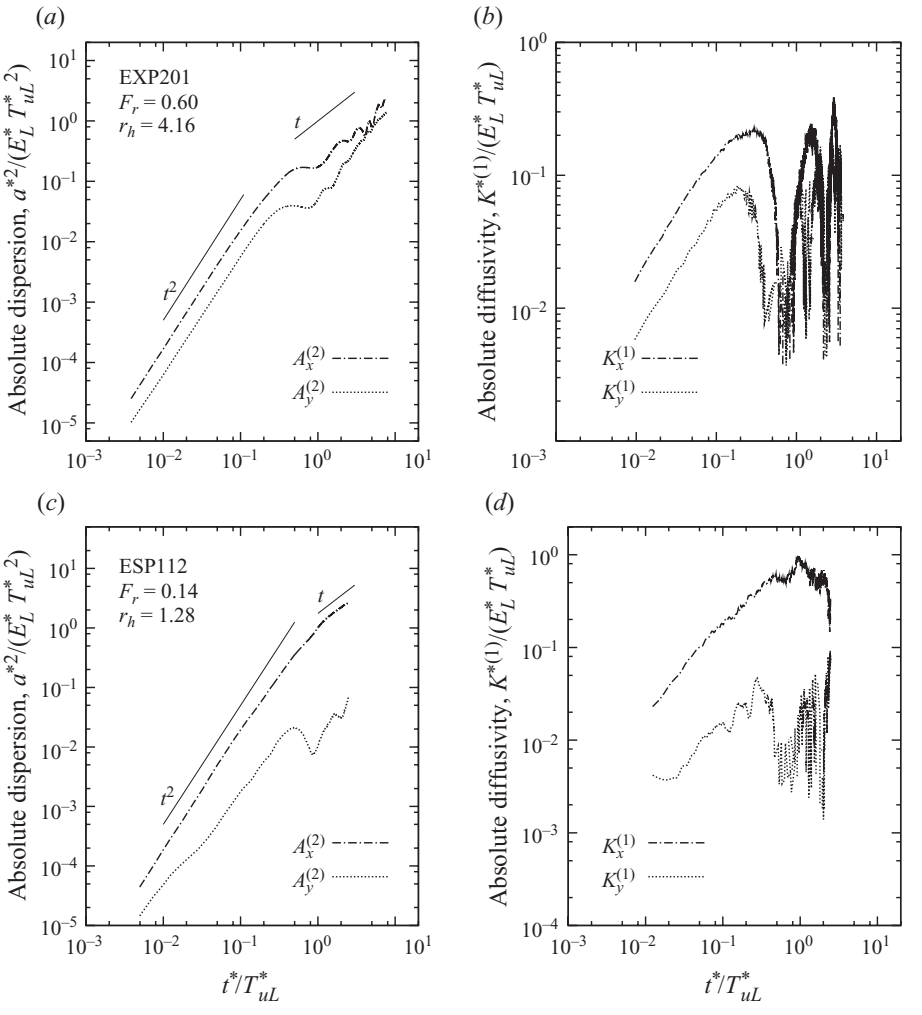

FIGURE 7. Plots of $A_x^{(2)}$, $A_y^{(2)}$, $K_x^{(1)}$ and $K_y^{(1)}$ for the shallow flow of EXP201 (a, b) and the deep flow EXP112 (c, d).

are unable to trigger significant mixing processes in the transverse direction (y), leading to a stronger anisotropy with a difference of approximately one order of magnitude.

4.3. *Multiple-particle statistics*

Further information on the mixing processes can be gained by analysing multiple-particles statistics in terms of relative quantities, p.d.f.s of the particles separations and FSLEs. In the following, we discuss these quantities for the three flow classes separately. From such an analysis, different scenarios, depending on the value of r_h and Fr, arise.

4.3.1. *Shallow flows*

The behaviour of the relative diffusivity $K^{(2)}$ versus the initial separation $r = r^*/L_{uL}^*$ is shown in figure 8; as postulated by Bennett (1984), relative diffusivity follows a power law of the type $K^{(2)} \propto r^{\beta}$. Note that the computation of the relative diffusivity is performed by time differentiating the squared separation $r^2(t)$, which has

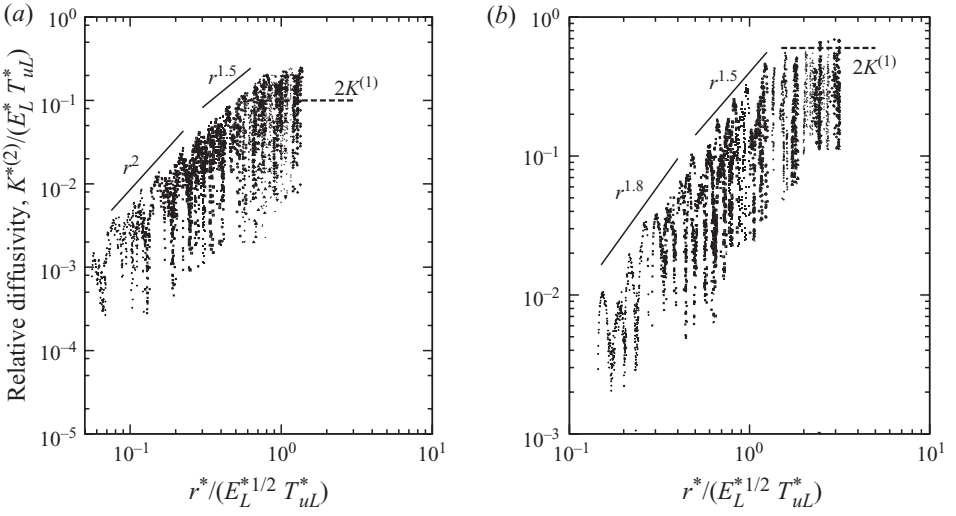

FIGURE 8. Relative diffusivity as a function of the dimensionless separation r for shallow flow conditions ($r_h > 3$): (*a*) EXP101 and (*b*) EXP201.

small-amplitude high-frequency oscillations. Therefore, the time derivative becomes a rather noisy signal. However, the trend of the envelope of the relative diffusivities for different initial separations allows an identification of power law in $r(t)$.

In the case of shallow flow conditions, the results suggest that the growth of the relative diffusivity follows two distinct power laws depending on the scale of the separation, namely for small separation $K^{(2)} \propto r^{1.8\text{–}2.0}$ and large separation $K^{(2)} \propto r^{1.5}$. The change of the growth regime seems to occur for distances smaller than the spatial integral scale (L_{uL}^*, i.e. $r = 1$), suggesting the existence of another length scale that plays a significant role in the mixing dynamics. More precisely, the regime with exponent 1.8–2.0, which we regard as the first indication of a direct enstrophy cascade, persists as long as the particle separations remain below the values of 0.2 for EXP101 and 0.4 for EXP201 (see figure 8). These approximately correspond to the turbulence 'injection length scale' L_i that has already been highlighted to be the typical scale of generation of vorticity (hence turbulence) in a compound channel flow (Stocchino & Brocchini 2010). Note that, typically, it is $0.2L_{uL}^* \leqslant L_i^* \leqslant L_{uL}^*$. We postulate that for $r < L_i$, $K^{(2)}$ increases as would occur for a direct enstrophy cascade regime while for $L_i < r < 1$, $K^{(2)}$ increases at a lower rate (1.5) which we postulate to be compatible with an inverse energy cascade process (classical rate of 4/3).

In more detail, particle pairs initially separated by a distance smaller than L_i will experience both growth regimes, i.e. exponential in time ($K^{(2)} \propto r^2$) for $r < L_i$ and cubic in time ($K^{(2)} \propto r^{1.5}$) for $r > L_i$, whereas particle pairs with initial separation greater than L_i will grow cubically in time up to the largest scales of the flow.

An inverse energy cascade is the result of a specific dynamics of coherent vortical structures that undergo vortex merging, transferring in this way energy from the smaller to the larger scale. Indeed, vortex merging has been observed during the experiments run with shallow flow conditions, as shown in figure 9, where contours of the Okubo–Weiss eigenvalue of consecutive flow fields are displayed. Being aware that the detailed merging mechanism is still an open issue, which is beyond the scope of the present study, λ_0 has been used only for the purpose of helping the identification of the merging of the vortices. For convenience, we have plotted only the negative contours of

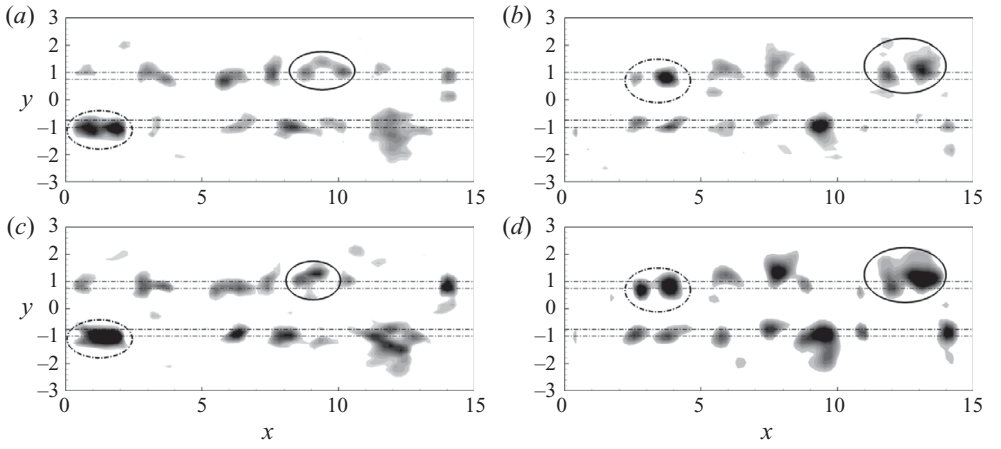

FIGURE 9. Contours of the Okubo–Weiss eigenvalue λ_0 showing vortex merging in the case of a shallow flow (EXP201, $r_h = 4.16$, $Fr = 0.60$). Merging events are highlighted by ellipses and occur around $(x, y) = (1, -1)$ and $(x, y) = (9, 1)$ at two subsequent times (a, c) and around $(x, y) = (3, 1)$ and $(x, y) = (13, 1)$ at two subsequent times (b, d). The dotted black lines indicate the transition regions of the compound channel. Note that only negative values of λ_0 have been displayed.

λ_0 that correspond to elliptical regions (vortices). It can be seen that vortices residing in the transition regions merge together, leading to larger flow structures. Further evidence of the presence of an inverse energy cascade occurring in shallow flow conditions can be found by means of the dimensionless Eulerian power spectral density (PSD) function $S_u(k^* L_i^*)$ of the streamwise (u) velocity component, where the wavenumber k^* has been made dimensionless using $W_{tr}^* = L_i^*$. The PSD functions have been normalized with the friction velocity u_* defined as $u_* = \sqrt{g h_{mc}^* S}$. Owing to the limited size of the velocity series in space, the computation of the PSD has been carried out in terms of frequency $S_u(f^*)$ and, subsequently, evaluated in terms of wavenumbers by dividing each frequency by the time and space-averaged surface velocity U_s^*, $k^* = f^*/U_s^*$, under the assumption of 'frozen turbulence', as suggested by Nikora *et al.* (2007) in a similar context of free-surface flows. Examples of dimensionless PSDs are reported in figure 10 for the shallow flow cases (EXP101 and EXP201). The figure illustrates the coexistence of two different regimes, separated at around $k^* L_i^* = k^* W_{tr}^* = 1$, i.e. at an injection scale comparable with the transition region width W_{tr}^*.

Additional information on dispersion dynamics can be gathered from the analysis of the p.d.f.s of the particles' displacements. The main advantage of using the time dependence of the p.d.f.s is the possibility of distinguishing different dispersion regimes characterized by the same dependence of $K^{(2)} \propto r^{\gamma}$ on the basis of the Gaussianity/non-Gaussianity of the p.d.f.s. Generally, the analysis of time dependence of the kurtosis should agree with the results obtained in terms of relative diffusivities, beyond providing additional information on the characteristics of the dispersion regimes (LaCasce 2008). For shallow flows, the kurtosis as a function of time, and the p.d.f.s at a dimensionless time equal to $t = t^*/T_{uL}^* = 2$ are shown in figure 11. The two regimes found on the basis of the results of relative diffusivity are characterized by two different behaviours of the kurtosis. Separations smaller than the injection scale ($L_i = 0.36$), namely $r_0 = 0.14$ and $r_0 = 0.21$, are characterized by a large values of ku, which is almost constant for times longer than the integral time scale ($t = 1$) and far from the Gaussian conditions, see p.d.f. distributions (figure 11*b*). On the contrary,

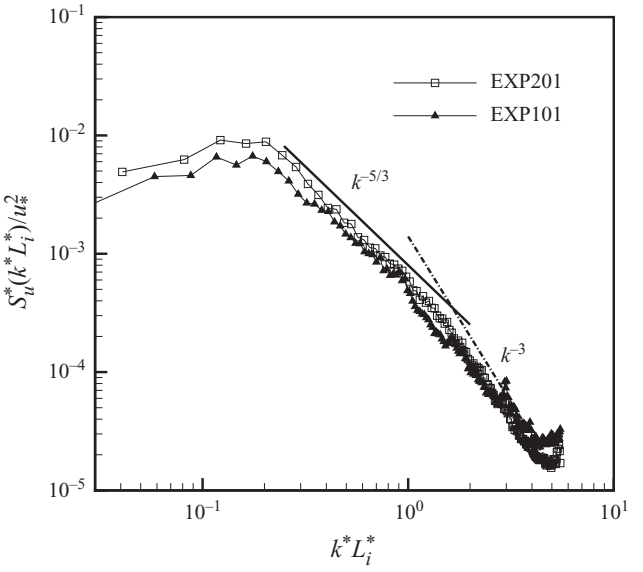

FIGURE 10. Normalized Eulerian PSD function S_u corresponding to the shallow flow experiments of figure 8.

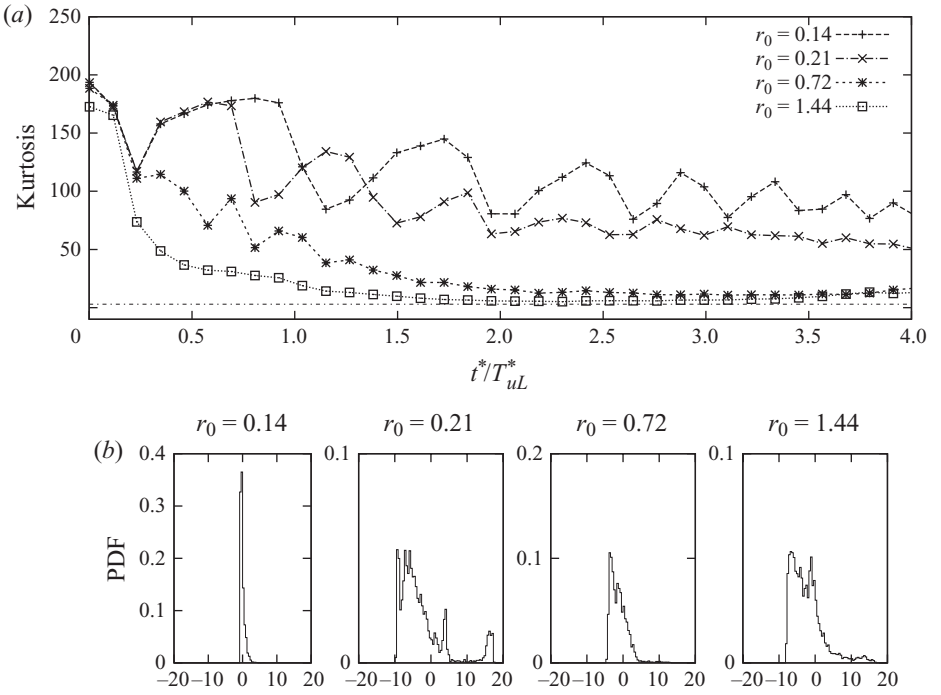

FIGURE 11. (*a*) Kurtosis of different initial relative separations (r_0) as a function of time. The dash-dotted line indicates the value of the kurtosis for a Gaussian distribution, i.e. $ku = 3$. (*b*) P.d.f. of relative displacements for dimensionless time ($t = 2$). Shallow flow (EXP201).

larger separations ($r_0 = 0.72$ and $r_0 = 1.44$), after an initial rapid decrease of ku, become quasi-Gaussian with a value of ku slightly larger than 3. The corresponding p.d.f. distributions possess, in this case, rounder peaks and shorter, thinner tails.

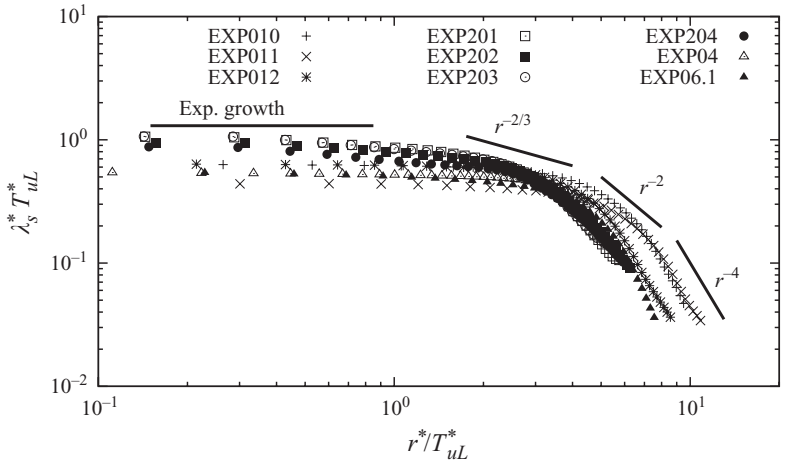

FIGURE 12. Finite-scale Lyapunov exponents (FSLEs) for shallow flow conditions.

The analysis of the relative statistics suggests that an equilibrium (Brownian) regime, where $K^{(2)} \propto 2K^{(1)}$, is attained for any value of r_h and Froude number once dimensionless separations are larger than 2. However, the results in terms of relative statistics are affected by strong oscillations. As already mentioned in § 3, this may be due to the accuracy in computing relative quantities at large scales. An alternative approach is to use the distance as the independent variable and average the times of mixing. In other words, the FSLEs are obtained by recording the times required for individual pair separations to increase from one distance to the next, as explained in § 3. Also, the results obtained by means of the FSLE should agree with those obtained by means of the relative diffusivity. In the specific case, they also highlight the presence of two distinct stages of growth: at the smaller scales the value of λ_s^* typically attains an almost constant value, while, once larger scales are reached, it decreases, following an approximate power-law dependence with the distance. In figure 12, the values of the FSLEs have been reported for shallow flow conditions. If the FSLEs attain a constant value over different separation scales, an exponential growth is implied. Indeed, the regime for separation smaller than the injection scale results in an exponential time growth of r^2, leading to an almost constant value of the FSLEs. For scales larger than $r = r^*/L_{uL}^* > 1$, the FSLEs suggest another phase of growth, and their values decrease with an approximate power law close to $r^{-2/3}$ as for the Richardson regime. Finally, for larger separations, the decay of λ_s follows a power law proportional to r^{-2}, suggesting the presence of an equilibrium regime (linear growth in the relative dispersion, i.e. the asymptotic regime characterized by standard diffusion, see LaCasce 2008 for more details).

Moreover, for separations larger than the equilibrium regime, the decay of the FSLEs becomes steeper, corresponding to a growth in time of the separations with an exponent less than unity ($\gamma < 1$). The latter result, indicating the existence of a subdiffusive regime, implies that particles remain trapped by the large-scale flow structures and, as a consequence, the dispersive process is inhibited by them. In the present case, however, this happens at scales comparable with the width of the channel, which represent a constraint on the particle separations. Therefore, the observed diffusive regime is only controlled by the geometrical characteristics of the experimental flume.

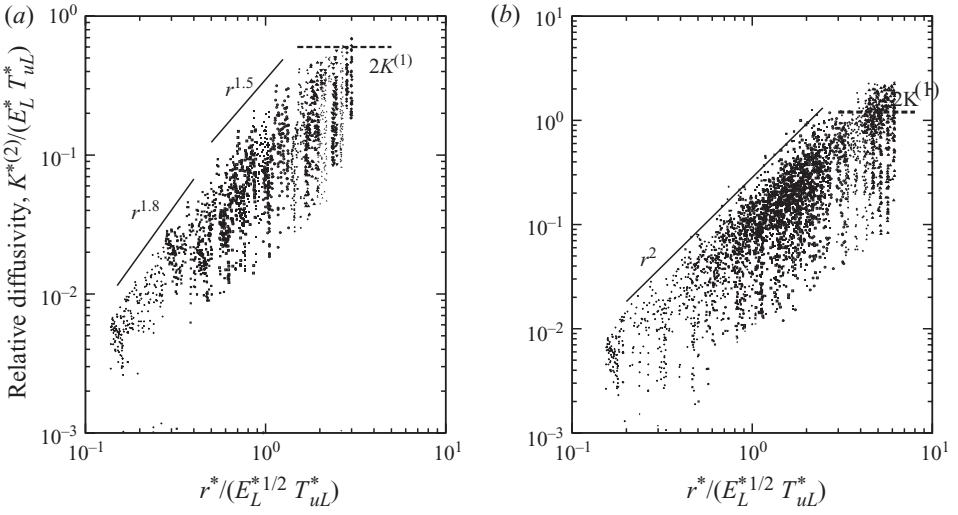

FIGURE 13. Relative diffusivity as a function of the dimensionless separation r for intermediate conditions ($2 < r_h < 3$) in different regimes: (a) subcritical flows, $Fr < 1$ (EXP205), and (b) supercritical flows, $Fr > 1$ (EXP12).

4.3.2. *Intermediate flows*

By decreasing r_h and entering the intermediate flow conditions, the dynamics of particle pairs is further complicated by the role of the Froude number. Intermediate flows behave quite differently from shallow flows although the influence of the macrovortices is still evident because of the simultaneous presence of transitional vortices and floodplains vortices, as already discussed in Stocchino & Brocchini (2010).

To highlight the role of the Froude number, the behaviour of $K^{(2)}$ as a function of the particle pair separation r is shown in figure 13, both for the subcritical regime ($Fr < 1$) and the supercritical regime ($Fr > 1$). In the former case, a strong similarity exists with the shallow flows, characterized by two distinct growth regimes (direct enstrophy cascade for $r < L_i$ and inverse energy cascade for $L_i < r < 1$, with $L_i \sim 0.36$). However, as the Froude number exceeds unity, our results indicate a change in the dynamics of the relative diffusivity with a single intermediate regime such that $K^{(2)} \propto r^2$, which is usually related to a non-local dynamics of particle pairs in the enstrophy inertial range associated with an energy spectrum of the kind $E(k) \propto k^{-3}$. Therefore, it seems that only for subcritical conditions, does an inverse energy cascade survive (the injection scale always related to the flow depth jump as in the shallow flow conditions), whereas only an enstrophy cascading process occurs for $Fr > 1$.

These behaviours are clearly evident by inspecting figure 14, where the results for the PSD functions are reported for the intermediate flow conditions. In particular, the subcritical case (figure 14a) is similar to that characterizing the shallow flows (see figure 10), whereas the supercritical case (figure 14b) shows an enstrophy cascade. In the latter case, it is reasonable to state that the flow is mainly dominated by the large-scale shear structure, rather than by the transitional macrovortices, so the dispersion is controlled by non-local processes.

A similar behaviour is observed in the p.d.f.s for subcritical intermediate flows, as shown in figure 15, where the inverse energy cascade is still the dominant process

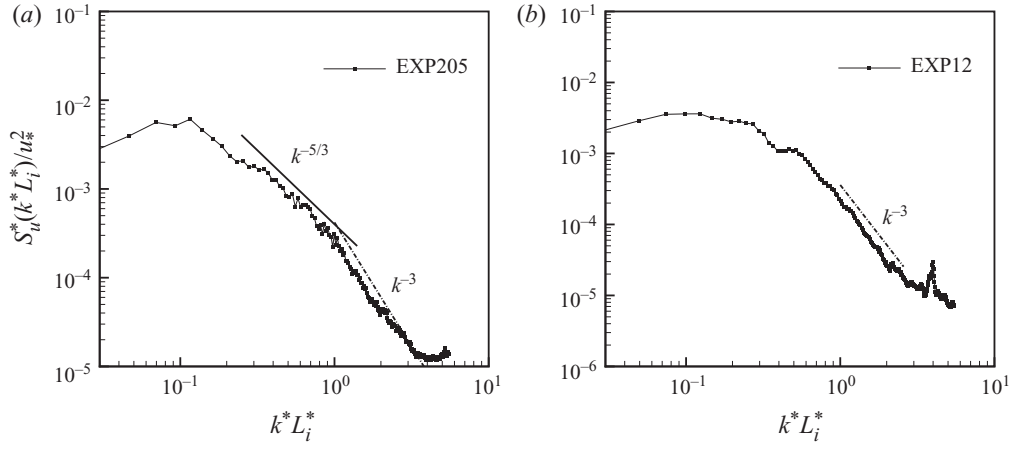

FIGURE 14. Normalized Eulerian PSD function S_u corresponding to the intermediate flow experiments of figure 13.

that controls the relative separation. Again, the smaller separations are clearly distinguished from the larger ones because the former are characterized by larger kurtoses, although in both cases ku attains almost constant values. However, if the flow regime is supercritical, the growth of the relative diffusivity $K^{(2)}$ follows one single power law (r^2) for any given initial value of the separations. The corresponding ku, after an initial decay stage lasting for $0 < t < 1.5$, rapidly tends to a constant value, approximately equal to 10, as observed for the large separations in the subcritical flows.

Similar to the shallow flow case, we have analysed the behaviour of the values of the FSLEs for different separations. In figure 16(*a,b*), the results obtained for the intermediate flows for subcritical and supercritical conditions are reported. In the case of subcritical conditions, results similar to those shown for shallow flows are recovered: for small separations, it is possible to identify a first regime corresponding to an almost constant slope, while for larger separations a Richardson-like regime ($r^{-2/3}$) and an equilibrium regime (r^{-2}) are found. For supercritical flow conditions, when an enstrophy cascade sets in and $K^{(2)}$ follows a single trend proportional to r^2 (which implies an exponential growth in time of r^2), the plateau of λ_s extends up to $r \simeq 2$. For larger separations, an equilibrium is again reached. Also, in this case a subdiffusive regime is visible for separations larger than $r > 5$.

4.3.3. *Deep flows*

The relative diffusivity always follows one single growth power law which, however, depends on the flow regime, i.e. $K^{(2)} \propto r^{1.5}$ in the subcritical regime and $K^{(2)} \propto r^2$ in the supercritical one (see figure 17).

Even in this case, the equilibrium phase is not easily detectable from $K^{(2)}$. A single growth regime is also evident from the FSLEs, see figure 18. Indeed, the exponential growth is almost absent in the case of subcritical flows, where a single trend proportional to $r^{-1/3}$ covers separations up to about 3, before changing to a clear equilibrium slope (r^{-2}). On the contrary, supercritical flows are characterized by a long exponential growth, related to $K^{(2)} \propto r^2$, again followed by a diffusive regime.

An explanation for the behaviour of the deep flows is based on the observation that the topographic forcing only weakly affects such a flow, since $r_h \to 1$ and, as a consequence, no transitional vortices are observed. The results suggest that for

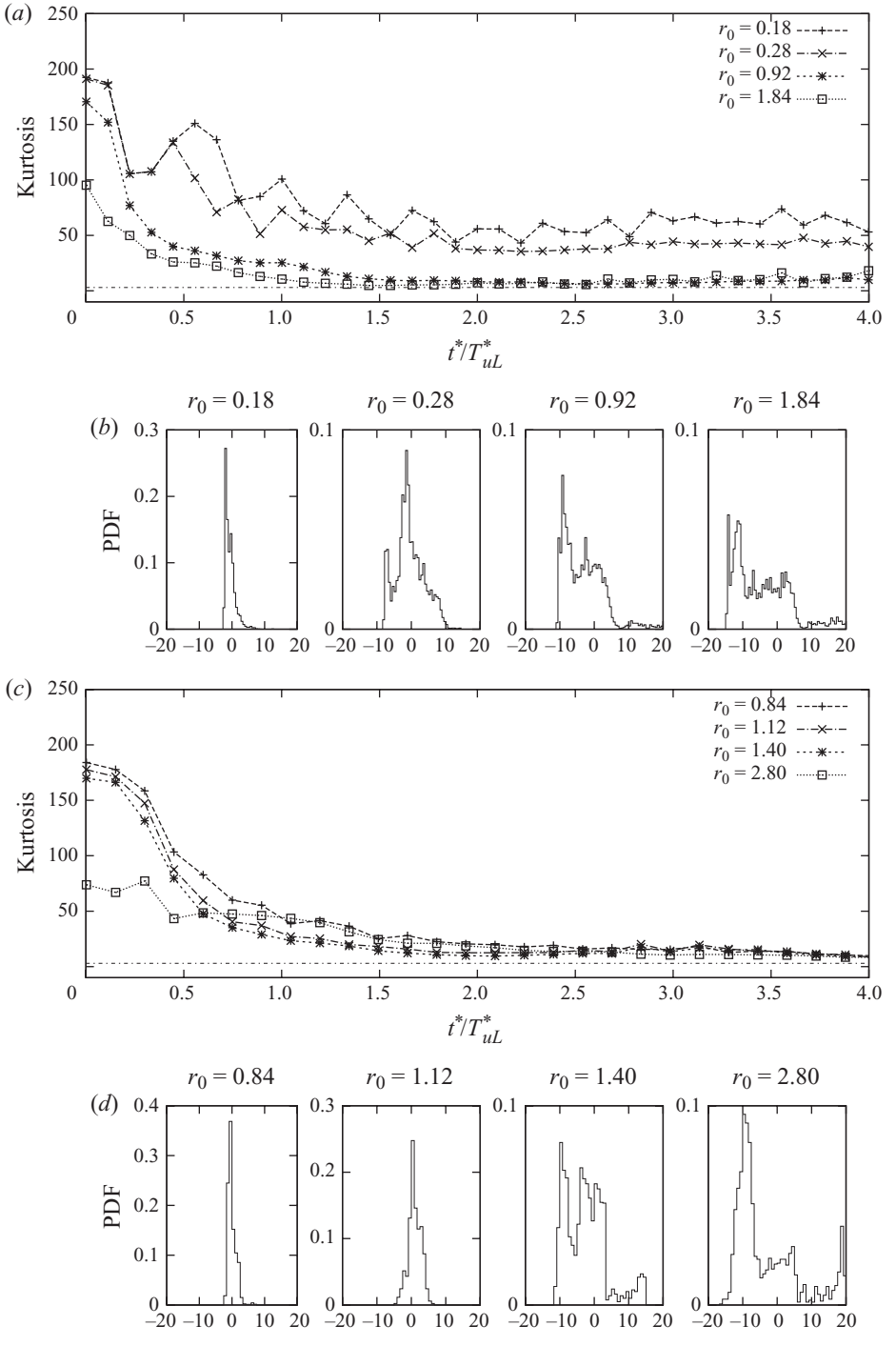

FIGURE 15. (a, b) Subcritical (case EXP205) and (c, d) supercritical (case EXP12) intermediate flows. (a, c) Kurtoses of different initial relative separations (r_0) as a function of time. The dash-dotted line indicates the value of the kurtosis for a Gaussian distribution, i.e. $ku = 3$. (b, d) P.d.f.s of relative displacements for dimensionless time ($t = 2$).

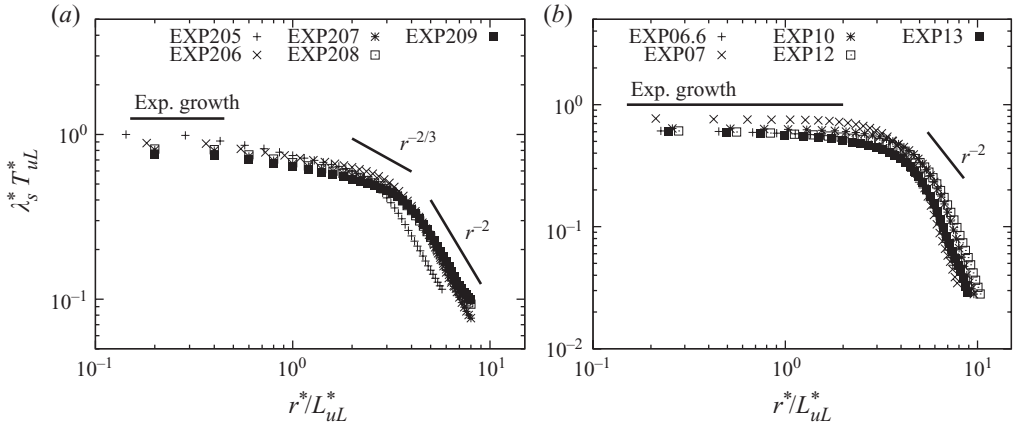

FIGURE 16. FSLEs for intermediate flow conditions. (*a*) Subcritical flow ($Fr < 1$) and (*b*) supercritical flow ($Fr > 1$).

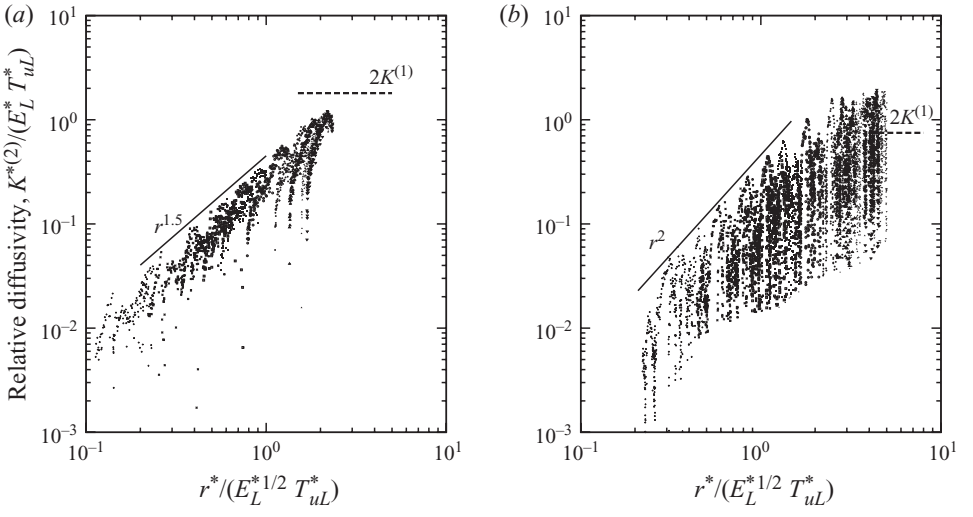

FIGURE 17. Relative diffusivity as a function of the dimensionless separation r for deep conditions ($r_h < 2$) in different regimes: (*a*) subcritical flows ($Fr < 1$) EXP112 and (*b*) supercritical flows ($Fr > 1$) EXP17.

subcritical flows, the energy transfer occurs through a direct energy cascading (see figure 19*a*) where for the PSD an exponent -2 is recovered (close to the value of $-5/3$ typical of a Richardson regime), whereas in the supercritical regime a direct enstrophy cascade dominates the dynamics (see figure 19*b*).

The present results are in good agreement with the findings of Nikora *et al.* (2007), who investigated the influence of large-scale flow structures on the energy processes characterizing free-surface uniform flows, in a case of rectangular cross-section. The analysis of the surface velocity measurements presented in Nikora *et al.* (2007) suggests that for $Fr > 1$, the energy spectrum follows a power law with an exponent -3 (enstrophy cascade) while, for subcritical conditions ($Fr < 1$), a direct energy cascade was observed. Note that the same exponent of the Richardson regime can also be recovered in the case of shear dispersion.

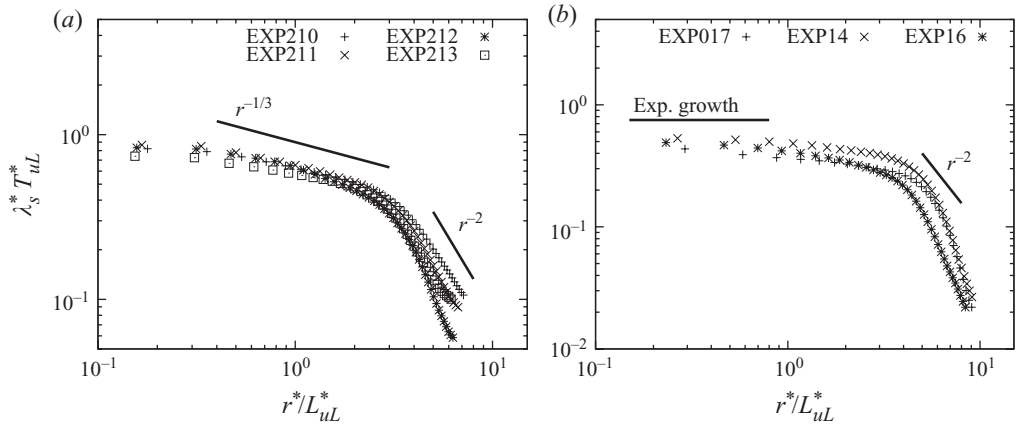

FIGURE 18. FSLEs for deep flow conditions. (*a*) Subcritical flow ($Fr < 1$) and (*b*) supercritical flow ($Fr > 1$).

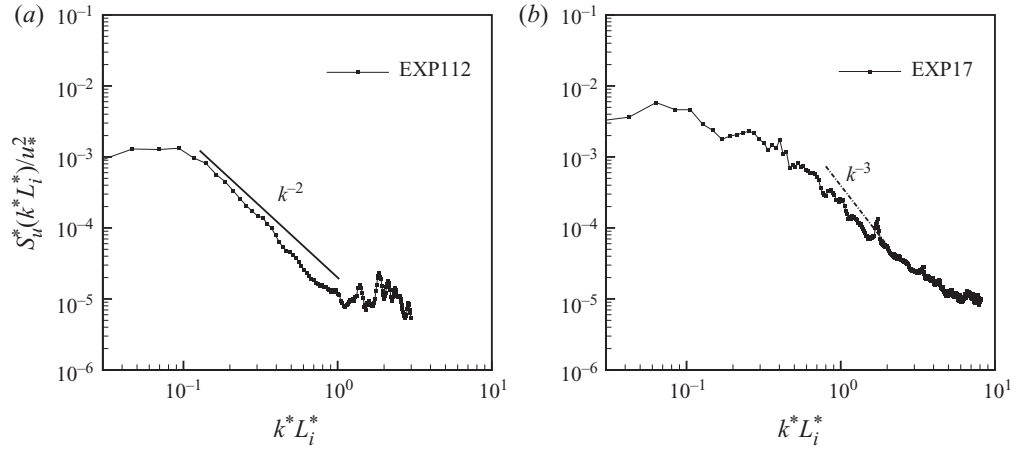

FIGURE 19. Normalized Eulerian PSD function S_u corresponding to deep flow experiments of figure 17.

For the present case, shear dispersion is likely to occur in the case of deep flows. A way to distinguish the Richardson dispersion from shear dispersion is to investigate the p.d.f.s of the separations, since in the case of shear dispersion p.d.f.s of separation should be Gaussian (LaCasce 2008). Subcritical deep flows are characterized by a Richardson-like exponent; however, the time dependence of the kurtosis, after an initial decay stage for $0 < t < 1.5$, attains an almost constant value close to pure Gaussian distributions ($ku = 3$), suggesting that in these conditions a shear dispersion takes place (Bennett 1987) (see figure 20*a, b*). Finally, in supercritical flows the results are in agreement with those found for the supercritical intermediate flows, i.e. ku decays from its initial value to a constant value approximately equal to 10 (see figure 20*c, d*).

5. Conclusions

An extensive laboratory campaign has been dedicated to the analysis of the Lagrangian mixing of straight compound channels in quasi-uniform flow, for different conditions described by the values of the main physical parameters (r_h and Fr).

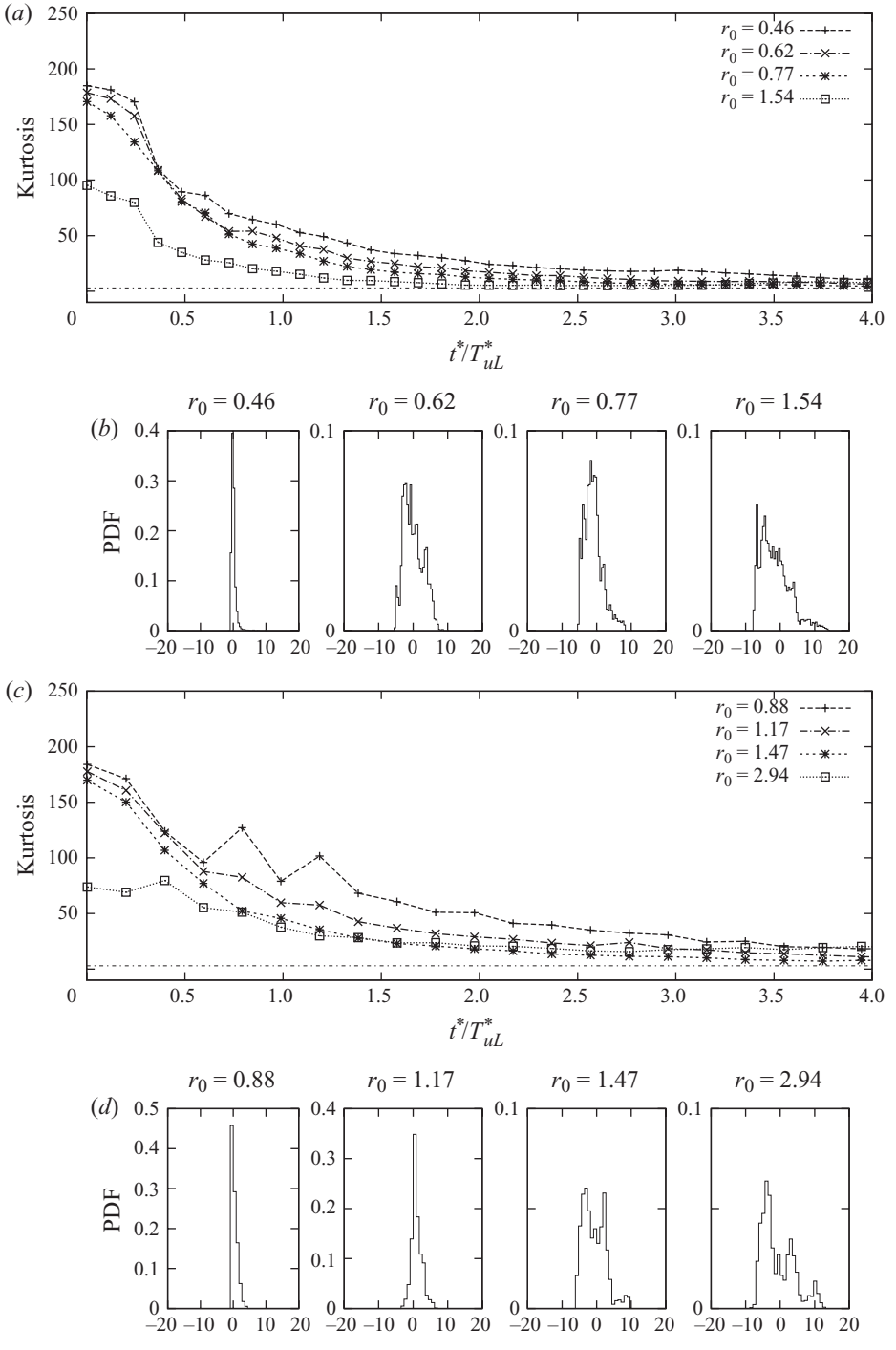

FIGURE 20. (*a, b*) Subcritical (case EXP213) and (*c, d*) supercritical (case EXP17) deep flows. (*a,c*) Kurtoses of different initial relative separations (r_0) as a function of time. The dash-dotted line indicates the value of the kurtosis for a Gaussian distribution, i.e. $ku = 3$. (*b, d*) P.d.f.s of relative displacements for dimensionless time ($t = 2$).

The main conclusions of the study are the following.

(i) For large values of the flow depth ratio ($r_h > 3$), the dominant flow features are the quasi-two-dimensional vortical structures known as 'macrovortices', which are mainly concentrated in the transition regions where the flow depth jump is localized. These macrovortices strongly influence the total absolute dispersion (a^2) that is characterized by a non-monotonic growth with time in the regime intermediate between a small-time ballistic regime and an asymptotic Brownian regime. In particular, a local maximum is found, after the initial ballistic regime, for times comparable with 2–3 times the mean turnover time. Decreasing r_h leads to a smoother growth of the total absolute dispersion with the classical asymptotic regimes predicted by Taylor (1921).

(ii) The macrovortices are also responsible for an intense dispersion in the spanwise direction, yielding comparable values of the absolute diffusivities ($K_x^{(1)}$ and $K_y^{(1)}$), whereas the almost absence of long-lived coherent structures in the deep flows leads to a stronger anisotropy.

(iii) As long as the transitional macrovortices are the dominant flow features, the results obtained for the relative diffusivity $K^{(2)}$ reveal two distinct growth regimes as a function of the particle separation: for scales smaller than the injection length scale, here coinciding with the size of the transition region, $K^{(2)}$ increases as it would for a direct enstrophy cascade process, whereas for scales larger than the injection scale, $K^{(2)}$ increases at a rate compatible with an inverse energy cascade. The latter finding is supported by observations of vortex merging events in the case of shallow flows.

(iv) For relatively low values of r_h, i.e. for intermediate flows, the dynamics of particle pairs is strongly influenced by the flow intensity measured as a function of a suitable Froude number. The dispersion regimes for subcritical intermediate flows are in agreement with those obtained for shallow flows (enstrophy cascade for $r < L_i$ and inverse energy cascade for $r > L_i$), whereas, once the Froude number is increased beyond the critical value of 1, the relative diffusivity is characterized by one single regime compatible with enstrophy cascading, suggesting the dominance of large-scale shearing rather than of transitional macrovortices.

(v) Decreasing further the value of r_h, i.e. reaching the deep flow conditions, since the topographic forcing is no longer effective in triggering the formation of the macrovortices, one single regime is obtained for both subcritical and supercritical flows. The values of the exponent of the growth laws suggest the presence of a direct enstrophy cascade for $Fr > 1$, whereas for $Fr < 1$ a direct energy cascade dominates the dynamics of mixing. For the latter case, the distinction between the Richardson-type mixing and shear dispersion, characterized by the same exponent of the growth of $K^{(2)}$, has been performed by analysing the high-order moments of the p.d.f.s of the separations. A value of the kurtosis close to 3 is related to a Gaussian distribution of the pair separation, indicating that the subcritical deep flows are characterized by a shear dispersion.

(vi) The analysis of the FSLE reveals an equilibrium regime for the whole set of experiments, regardless of the values of the physical parameters.

(vii) Larger separations show a subdiffusive regime that is induced by the geometrical constraints of the experimental flume.

The present analysis has shown that, despite the apparent simplicity of the flow investigated, i.e. regular geometry and uniform flow conditions, the associated Lagrangian mixing processes are rather complex and fundamentally controlled by two main parameters which are the flow depth ratio and Froude number.

Further analyses are needed to clarify the possible generation of time-dependent Lagrangian coherent structures (LCSs), which are recognized to be material elements with a strong influence on the mass transport (Boffetta *et al.* 2001). LCSs cannot be identified by using either single-particle or multiple-particle statistics, but only by means of tools which are typically employed in the analysis of nonlinear dynamical systems (see Wiggins 2005 for a complete review). This is the focus of an ongoing analysis which will be summarized in a forthcoming, dedicated manuscript.

This research has been partially supported by the Fondazione Cassa di Risparmio di Verona, Vicenza, Belluno ed Ancona, under the framework of the projects MODITE and RIMOF2. G.B. has been supported by the University of Genoa under the framework of the Research Project 'Ateneo 2010'.

REFERENCES

Babiano, A., Basdevant, C., Le Roy, P. & Sadourny, R. 1987 Single-particle dispersion, Lagrangian structures function and Lagrangian energy spectrum in two-dimensional incompressible turbulence. *J. Mar. Res.* **45**, 107–131.

Babiano, A., Basdevant, C., Le Roy, P. & Sadourny, R. 1990 Relative dispersion in two-dimensional turbulence. *J. Fluid Mech.* **214**, 535–557.

Bennett, A. F. 1984 Relative dispersion: Local and nonlocal dynamics. *J. Atmos. Sci.* **41**, 1881–1886.

Bennett, A. F. 1987 A Lagrangian analysis of turbulent diffusion. *Rev. Geophys.* **4**, 799–822.

Boffetta, G., Lacorata, G., Redaelli, G. & Vulpiani, A. 2001 Detecting barriers to transport: A review of different techniques. *Physica* D **159**, 58–70.

Davis, R. E. 1982 On relating Eulerian and Lagrangian velocity statistics: single particles in homogeneous flows. *J. Fluid Mech.* **114**, 1–26.

Davis, R. E. 1983 Oceanic property transport, Lagrangian particle statistics and their prediction. *J. Mar. Res.* **41**, 163–194.

Elhmaïdi, D., Provenzale, A. & Babiano, A. 1993 Elementary topology of two-dimensional turbulence from a Lagrangian viewpoint and single-particle dispersion. *J. Fluid Mech.* **257**, 533–558.

Er-El, J. & Peskin, R. L. 1981 Relative diffusion of constant-level balloons in the Southern Hemisphere. *J. Atmos. Sci.* **38**, 2264–2274.

Garcia-Olivares, A., Isern-Fontanet, J. & Garcia-Ladona, E. 2007 Dispersion of passive tracers and finite-scale Lyapunov exponents in the Western Mediterranean Sea. *Deep-Sea Res.* **54**, 253–268.

Guala, M., Liberzon, A., Tsinober, A. & Kinzelbach, W. 2007 An experimental investigation on Lagrangian correlations of small-scale turbulence at low Reynolds number. *J. Fluid Mech.* **574**, 405–427.

Hua, B. L. & Kline, P. 1998 An exact criterion for the stirring properties of nearly two-dimensional turbulence. *Physica* D **113** (1), 98–110.

Jirka, G. H. 2001 Large-scale flow structures and mixing processes in shallow flows. *J. Hydraul. Res.* **39**, 567–573.

Kraichnan, H. 1966 Dispersion of particle pairs in homogeneous turbulence. *Phys. Fluids* **9**, 1937–1943.

LaCasce, J. H. 2008 Statistics from Lagrangian observations. *Prog. Oceanogr.* **77**, 1–29.

Lekien, F., Coulliette, C., Mariano, A. J., Ryan, E. H., Shay, L. K., Haller, G. & Marsden, J. 2005 Pollution release tied to invariant manifolds: A case study for the coast of Florida. *Physica* D **210**, 1–20.

Lin, J. T. 1972 Relative dispersion in the enstrophy cascading inertial range of homogeneous two-dimensional turbulence. *J. Atmos. Sci.* **29**, 394–396.

Luo, J., Ushijima, T., Kitoh, O., Lu, Z. & Liu, Y. 2007 Lagrangian dispersion in turbulent channel flow and its relationship to Eulerian statistics. *Intl J. Heat Fluid Flow* **28**, 871–881.

Morel, P. & Bandeen, W. 1973 The EOLE experiment, early results and current objectives. *Bull. Am. Metereol. Soc.* **54**, 298–306.

Nezu, I., Onitsuka, K. & Iketani, K. 1999 Coherent horizontal vortices in compound open-channel flows. In *Hydraulic Modeling* (ed. V. P. Singh, I. W. Seo & J. H. Sonu), pp. 17–32. Water Resources Pub.

Nikora, V., Nokes, R., Veale, W., Davidson, M. & Jirka, G. H. 2007 Large-scale turbulent structure of uniform shallow free-surface flows. *Environ. Fluid Mech.* **7**, 159–172.

Okubo, A. 1970 Horizontal dispersion of floatable particles in the vicinity of velocity singularities such as convergences. *Deep-Sea Res.* **17**, 445–454.

Orre, S., Gjevik, B. & LaCasce, J. H. 2006 Characterizing chaotic dispersion in a coastal tidal model. *Contin. Shelf Res.* **26**, 1360–1374.

van Prooijen, B. C., Battjes, J. A. & Uijttewaal, W. S. J. 2005 Momentum exchange in straight uniform compound channel flow. *J. Hydraul. Engng* **131** (3), 175–183.

van Prooijen, B. C. & Uijttewaal, W. S. J. 2002 A linear approach for the evolution of coherent structures in shallow mixing layers. *Phys. Fluids* **14** (12), 4105–4114.

Provenzale, A. 1999 Transport by coherent barotropic vortices. *Annu. Rev. Fluid Mech.* **31**, 55–93.

Sellin, R. H. J. 1964 A laboratory investigation into the interaction between the flow in the channel of a river and that over its flood plain. *La Houille Blanche* **7**, 793–802.

Shiono, K. & Knight, D. W. 1991 Turbulent open-channel flows with variable depth across the channel. *J. Fluid Mech.* **222**, 617–646.

Socolofksy, S. A. & Jirka, G. H. 2004 Large-scale flow structures and stability in shallow flows. *J. Environ. Engng Sci.* **3**, 451–462.

Soldini, L., Piattella, A., Brocchini, M., Mancinelli, A. & Bernetti, R. 2004 Macrovortices-induced horizontal mixing in compound channels. *Ocean Dyn.* **54**, 333–339.

Stocchino, A. & Brocchini, M. 2010 Horizontal mixing of quasi-uniform, straight, compound channel flows. *J. Fluid Mech.* **643**, 425–435.

Taylor, G. I. 1921 Diffusion by continuous movement. *Proc. Lond. Math. Soc.* **20**, 196–212.

Weiss, J. 1991 The dynamics of enstrophy transfer in two-dimensional hydrodynamics. *Physica* D **48**, 272–294.

Wiggins, S. 2005 The dynamical system approach to Lagrangian transport in oceanic flows. *Annu. Rev. Fluid Mech.* **37**, 295–328.